Numerical Simulations of Small-scale and Full-scale Fire Experiments

by

Daniel Pegg Wilson

A thesis
presented to the University of Waterloo
in fulfillment of the
thesis requirement for the degree of
Master of Applied Science
in
Mechanical and Mechatronics Engineering

Waterloo, Ontario, Canada, 2018

This thesis consists of material all of which I authored or co-authored: see Statement of Contributions included in the thesis. This is a true copy of the thesis, including any required final revisions, as accepted by my examiners.

I understand that my thesis may be made electronically available to the public.

Statement of Contributions

Sections 3.1 - 3.2 consist of a condensed version of a paper that is co-authored by myself, my supervisor - Dr. Devaud, Dr. Weckman, and a former PhD student - Dr. Didomizio. My primary contribution is the development of the finite difference models and discussion of results. Dr. Didomizio completed the experimental work and provided support in formulation and analysis of the models.

Abstract

A fundamental part of fire safety engineering is dedicated to the application of numerical fire models. Accurate predictions of real-life fires are needed in scenarios related to fire growth, smoke propagation, occupant egress, and structural integrity. In the context of building safety, fire modelling tools can be used to predict the response of materials to fire situations, and are increasingly prevalent in performance based design.

In the present work, heat transfer and fire simulations are created with the objective to predict the resultant fire effects of different experiments. The simulations range in complexity from algebraic finite difference models to computational fluid dynamics (CFD) calculations. For each set of simulations, numerical predictions are compared with experimental data, whenever available. FireFOAM, an open source computational fluid dynamics solver, is selected as the modelling tool of choice. In the present study, four sets of simulations are conducted based upon experimental work. Firstly, a small scale test apparatus, the cone calorimeter, is investigated. Predictions from both a finite difference model and a CFD model compare favourably to the experimental results, and it is confirmed that a 1D finite difference model is not appropriate for the experimental configuration. Secondly, a full-scale fire experiment is investigated. The CFD simulations are extended to include the effects of turbulence and combustion. Large Eddy Simulation (LES) is selected for the turbulence modelling with a one equation eddy-viscosity model. Infinitely fast chemistry is assumed, and the eddy dissipation concept (EDC) is employed where combustion is controlled by the rate of turbulent mixing. Thirdly, a two-step reaction mechanism is implemented to account for compartment fires with under-ventilated combustion and more complex fuels. Chemistry based upon Arrhenius rate constants is assumed, and the Partially Stirred Reactor (PaSR) approach is employed. Good agreement is found for species and temperature predictions, with over-prediction of carbon dioxide concentrations due to modelling the reaction rates too fast. Finally, a preliminary CFD study is carried out for a multi-compartment fire where a wall section separates two compartments. Heat transfer is found to be over-predicted through the non-degrading wall section. To enhance the capabilities of the simulations, pyrolysis is recommended to be implemented to enable modelling of representative wall sections and realistic fuel loads.

Acknowledgements

I would like to thank my supervisor Cecile Devaud for her guidance and support throughout my degree. It has been a pleasure to work with her in both my research and teaching. I would like to thank Matt DiDomizio and Elizabeth Weckman for their advice and help with questions related to experimental work. I would like to thank my co-workers, Mohammad, Jeff, and Mehdi for the constructive discussion in the office and their advice over the past two years.

Funding from Natural Sciences and Engineering Research Council (NSERC) of Canada is gratefully acknowledged. Computations were performed on the GPC supercomputer at the SciNet HPC Consortium. SciNet is funded by: the Canada Foundation for Innovation under the auspices of Compute Canada; the Government of Ontario; Ontario Research Fund - Research Excellence; and the University of Toronto.

Table of Contents

List of Tables

List of Figures

Chapter 1

Introduction

1.1 Overview

Fire safety is an important consideration in the design of new buildings. The hazard of fire is a significant concern and special attention to modern type furniture and building materials is critical. For example, a room containing legacy furnishings was measured to take 700% longer to reach flash-over than modern rooms [42]. In this experiment, the modern rooms all flashed-over in less than five minutes from the time of ignition. Further, enclosed fires can pose a significant danger to the environment and occupants. Besides the heat effects, fire gases are produced, some of which are toxic, including carbon monoxide (CO), and nitrous oxides (NO_x) [68]. Building codes incorporate a certain amount of fire safety applied to doors, walls, and windows for the purposes of containing and slowing the spread of fire and smoke. Even with the attention to safety present in North America, the danger of residential fires is still as present as ever. This is due to the trend towards larger homes with increased fuel loads, new construction materials, and open concept homes. The average new home size has increased over 50 percent from the 1970's [42]. An additional danger is the transition to synthetic materials, which have significantly higher peak heat release rates (HRR) than legacy materials [42]. New construction materials tend to prioritize cost and installation time over fire safety. Open concept design reduces compartmentalization of the fire and increases the volume of air, which leads to increased flame and smoke spread. The combination of these characteristics lead to an increased risk of damaging consequences of fire events, and the importance of fire safety design.

Thus, there is a need for accurate predictions of the thermal environment within a compartment and the performance of contained materials in the case of fire. Typically, there

are two ways of obtaining these predictions — experimental tests and numerical modelling. Experiments are generally standardized and can range from small-scale to full-scale tests. One example of a small-scale experiment is cone calorimetry, where a representative section of material is heated under a cone heater, and the temperature and degradation characteristics measured. Full-scale experiments include compartment fires conducted within a standardized room geometry. Secondly, numerical modelling, specifically Computational Fluid Dynamics (CFD), is an approach which has become increasingly prevalent as computing power has improved, making the simulation of fire more achievable. Fire modelling allows for predictive simulations of fire events and is used in applications related to building codes, forensics, design, and life safety. However, Hosser and Hohm [37] identified a lack of fire simulations capable of evaluating both the gas and solid phase of a fire domain.

1.2 Objective

The objective of the current work is to develop fire simulations to predict the effects of a set of fire experiments, culminating in a multi-compartment fire simulation to predict the thermal environment in both the fluid and solid domains. The simulations are developed using fireFOAM [32], a solver implemented within the OpenFOAM CFD package [1]. The simulations are to be applied to both small and full-scale experiments, focusing on predictions of the flow field, temperature, and species concentrations. Based upon the accuracy desired and computational time, selection of specific models for radiation, turbulence, and combustion will be made. This study will also investigate different chemistry mechanisms to enable accurate simulations of compartment fires under different ventilation conditions.

1.3 Outline

This thesis consists of a chapter of background information followed by four chapters of simulations of fire experiments with increasing complexity. Throughout the development of the work, the numerical implementation of the main phenomena of heat transfer, turbulence, and combustion are investigated. As each new modelling technique or sub-model is introduced, a discussion of that model and rationalization is presented. Each subsequent chapter builds upon the work presented in the previous chapter.

Chapter 2 provides an overview of fire phenomena and compartment fire behaviors. As well, common fire experiments and available fire modelling software are discussed.

Chapter 3 presents the work done on simulations of small-scale experiments in two ways — a finite difference model and a CFD simulation. The objective of Chapter 3 is to create multi-dimensional models which can reproduce the results of a cone calorimeter test. Specifically, models to be applied to a novel non-standard configuration of the cone calorimeter apparatus. Tests are conducted on a non-degrading steel specimen, and temperature measurements are compared to predictions of heat transfer models. The finite difference models consist of one and two dimensional heat transfer calculation methods. The CFD simulations in fireFOAM also form a starting point for the development of full-scale CFD calculations. Numerical predictions are compared to experimental tests performed at the University of Waterloo Fire Research Lab.

Chapter 4 investigates compartment fires with specific attention to the temperature and flow profiles in the compartment. A methanol (CH_3OH) pool is burned in a large room with a single door opening. Temperatures and heat flux in multiple locations are available. Gas phase radiation, turbulence, and combustion are three models implemented in the CFD simulations. Numerical predictions are compared during both the growth phase of the fire and steady state.

Chapter 5 expands upon the CFD simulations in Chapter 4 and investigates a compartment fire under different ventilation conditions. The objective is to model a more complex fuel, heptane C_7H_{16}, with a higher degree of detail in the combustion and chemistry models. This is necessary to predict under-ventilated conditions where incomplete combustion occurs. The description of the experimental setup is outlined, as well as the reasoning for selection of the chemistry, reaction mechanism, and combustion model. Both temperature and species concentrations are compared, and a sensitivity study is completed on key model parameters.

Chapter 6 examines the wall effects in a multi-compartment domain. The objective is to create a simulation that can incorporate multiple compartments and the dividing materials between them. An experiment is selected in which wood cribs are the fuel, and a steel wall divides two compartments. In this chapter, a preliminary investigation is completed that does not incorporate pyrolysis. Temperature predictions are compared within both compartments and at multiple locations on the steel wall. Finally, recommendations are made for further extending the capabilities of the simulations.

Chapter 2

Background

Fire is defined as an "uncontrolled chemical reaction producing light and sufficient energy" [60]. It is a source of energy that can be harnessed and utilized in many productive ways. From providing heating for warmth and food in the early days of human history to powering vehicles and power plants in the modern world. However, uncontrolled fire can have devastating impacts. Destructive events can be naturally occurring or as a result of human activities. The most common example of naturally occurring fire are forest fires. Thermal weapons and residential fires are the result of human action or negligence. These events can cause injury and death on a large scale and millions of dollars in property loss. An early example is the Great Fire of London, where the vast majority of homes were destroyed within the city of London, England in the 17th century [58]. The Great Chicago Fire left 1/3 of residents without homes, due to the wood construction and flammable roofs [36]. Even today, there are examples of poor fire safety construction due to inadequate design or cost cutting efforts. Recently, the Grenfell Tower fire in England resulted in significant casualties due to poor design of the exterior cladding and evacuation routes [15]. Fire knowledge is always evolving and expanding. For example, it was common practice for firefighters to open up doors, windows, and roofs to ventilate uncontrolled compartment fires with the goal of releasing heat from the compartment. Due to fire research and testing the opposite is now done. Doors are closed to prevent the fire from receiving enough oxygen (O_2) to fuel itself. Understanding fire and how to mitigate or minimize its effects are critical in today's society, both from a prevention and fire fighting point of view.

In the present chapter, an overview of the key physical phenomena taking place in a fire is presented, then a summary of common fire tests which will be referenced throughout this thesis is given, and finally the concept of fire modelling is introduced.

2.1 Fire Dynamics

Fire dynamics is the study of fire, specifically how fires start, spread, and develop. Fire is a result of a complex interaction of chemistry, heat transfer, and fluid dynamics. The physical phenomena present in a typical fire are reviewed in the subsequent sections.

2.1.1 Combustion

Combustion is a phenomenon that occurs from the reaction of gaseous fuel and O_2 at elevated temperatures. Flames are generally present as a result of the light produced by the combustion process. Combustion can be simply defined as the burning of fuel. For combustion to initiate, or be sustained, three components are required: O_2, heat, and fuel. These three components are commonly referred to as the "fire triangle". Depending upon the fuel and O_2 amounts present, either complete combustion or incomplete combustion may occur. For many beneficial applications, complete combustion is desired as the only products are carbon dioxide (CO_2) and water vapour (H_2O). Incomplete combustion occurs when the O_2 supply is limited, producing undesirable products including CO, carbon (soot), and other species including NO_x and hydroxides (OH) [28].

2.1.2 Pyrolysis

Pyrolysis is a chemical process at elevated temperatures. Liquid or solid fuels are decomposed into combustible gases due to a temperature increase within the fuel from a heat source. These gases then mix with air to form a combustible mixture which burns near the surface of the original fuel. It is not the solid or liquid fuel itself burning, as it may appear for an observer. Common examples include wood fires, and liquid fuel spills. Pyrolysis is a complex phenomena when fuels are heterogeneous in nature. Wood is comprised of many constituent products (cellulose, hemi-cellulose, lignin, ash) which each have their own thermophysical properties and degradation behaviour [88]. In the case of wood, the virgin material breaks down into char, tar, and volatile gases under the application of elevated temperatures. This process begins at approximately 200°C and progresses until approximately 500°C depending on the exact constitution of the material [69]. Pyrolysis is a critical mechanism to understand and predict as it is present in all fire scenarios. In residential fires, most furnishings comprised of plastic or wood undergo pyrolysis and then combustion.

2.1.3 Heat Release Rate

The most important value in which to classify fire is the HRR ($\dot{Q} = \dot{m}\Delta h_c$), where $\dot{Q}$ is the amount of energy released per unit time, $\dot{m}$ is the burning rate of the fuel and Δh_c is the heat of combustion (amount of energy released per mass) [12]. The HRR provides an indication of fire size, strength, and risk. The HRR is used to characterize materials, quantify hazard risk, and determine detector response times. As the HRR increases, related fire effects also increase, including smoke production, radiant energy, and toxic products of combustion.

2.1.4 Turbulence

Fluid flow can generally be classified as either laminar or turbulent. For the same geometry, laminar flow is flow at lower speeds while turbulence occurs at higher speeds. Laminar flow behaves predictably with negligible amounts of mixing. Turbulence generally occurs at higher speeds and is more chaotic and unstable in nature. Turbulence influences the reaction rate of the combustion process. Turbulence is representative of most engineering flows, including fire. Turbulent flow has characteristics of increased mixing and heat transfer properties. Turbulence is a process that has random fluctuations and can be difficult to predict the behaviour. Thus, instantaneous turbulence quantities are commonly decomposed into mean values and turbulence fluctuations [57].

For any numerical simulation there are three main turbulence approaches: direct numerical simulation (DNS), large eddy simulation (LES), and Reynolds-averaged Navier Stokes (RANS) [80]. DNS directly solves the Navier Stokes equations which govern fluid flow. This is the most theoretically accurate approach but has a very large computational overhead in most cases. Simple flows and low Reynolds number flows may be solved this way, however with current computational resources it is unsuitable to typical engineering flows. LES solves the larger scales of turbulent motion; where the bulk of the turbulent kinetic energy exists. The smaller scales are modelled and are more uniform in nature. A scale refers to the representative size of eddies formed due to unsteadiness in the flow. The LES approach includes some modelling compared to DNS but greatly reduces the computational resources needed. Finally, the RANS approach models all turbulent scales and is currently the most common turbulence approach selected in general engineering problems due to its proven reliability and lower computational resource requirement [57].

2.1.5 Heat Transfer

Heat transfer will occur whenever a temperature difference exists and heat will move from areas of high temperature to areas of low temperature. There are three modes of heat transfer: radiation, convection, and conduction. Fire primarily uses two of these modes: radiation and convection. In large fires, radiation dominates, in small fires convection dominates [28]. Radiation is a heat transfer phenomenon where energy is transmitted through electromagnetic waves. Neither contact or a medium is needed between the objects which have a temperature difference. An example is heat from the sun, transmitted through the vacuum of space. As shown in Eq. 2.1 radiation is dominant at high temperatures due to the quartic relation to temperature (T^4). Radiation generally dissipates the energy from a fire, which lowers the gas temperatures as it transfers energy from the burning area to the surroundings.

$$q_{rad} = \varepsilon \sigma A (T_2^4 - T_1^4), \tag{2.1}$$

where q is the energy transferred, ε is the total emissivity of the specimen surface, σ is the Stefan–Boltzmann constant (5.6704×10^{-8} $\mathrm{Wm^{-2}K^{-4}}$), A is the surface area of the emitting surface, and T_1 and T_2 are the surface temperatures of the emitting and absorbing surfaces, respectively [14].

Convection is heat transfer due to movement of a fluid over a solid. In the case of fire, movement of hot air transfers its heat to the surroundings. Eq. 2.2 represents the net rate of convective heat transfer into a surface.

$$q_{conv} = h_c A \left(T_g - T_s\right), \tag{2.2}$$

where h_c is the convective heat transfer coefficient between a surface and the adjacent gases and T_g is the gas temperature.

While conduction is the least significant heat transfer mode in fire, it still plays a role in many cases. Conduction is heat transfer due to contact between objects (solids, liquids, gases), but dominant in solids. With regards to fire scenarios, the surface of the material will be heated due to radiation and convection. Through conduction heat is transferred into the material. A common example would be firefighter bunker gear. The fabric surface will become very hot when exposed to fire conditions, however the suits are designed to reduce the conduction heat transfer, insulating their bodies form becoming too hot. As shown in Eq. 2.3 the heat transfer is dependent upon the contact area, length of material, and k, the thermal conductivity of a material. Thermal conductivity regulates how much heat is conducted through a material.

$$q_{cond} = \frac{k}{L} A \left(T_2 - T_1\right). \tag{2.3}$$

Another example of conduction is in walls enclosing a fire compartment. The amount of heat transferred into and through the wall is determined from the characteristics of the material and construction.

2.1.6 Wall Construction

Walls provide an important barrier to fire spread in compartment fires. Solid materials have three properties of importance; thermal conductivity, specific heat capacity, and density. Specific heat is the amount of heat needed to raise the temperature a certain amount, and density is the mass per unit volume. These three properties can be combined into a thermal diffusivity value ($\alpha = k/\rho c_p$). The higher the diffusivity value, the higher the propensity to conduct heat [28]. Walls are typically made of three components; drywall, insulation, and wood studs. Drywall is gypsum plaster sandwiched between two layers of thick paper. Gypsum is a mineral which is non-combustible, but rather undergoes dehydration when heated which releases the entrained water. The release of water provides good fire resistance characteristics due to its high heat capacity value. The principle is that the water absorbs heat from the fire, dissipating the amount of energy available. The primary purpose of insulation is to provide a barrier to maintain the temperature within the room by limiting the heat transfer within them. A secondary purpose is to prevent and contain the spread of fire. Insulation has a low thermal diffusivity as a result of the low thermal conductivity. It is generally made of fibrous material which contains a significant amount of air. Air serves as a good insulator as it does not conduct heat well. Finally, wood studs are a thermally degrading material which burn, however they are in place to provide structurally support to buildings. In terms of fire resistance, different types and construction of wood have a range of abilities depending on the mass and moisture content.

2.1.7 Compartment Fire Stages

A compartment fire refers to any fire in an enclosed space. This encompasses residential fires, industrial fires, and vehicle fires including bus, airplanes, and trains. It is important to gain a better understanding of fire dynamics and characteristics present in these situations, for the purposes of fire safety design.

Ignition To initiate combustion heat, fuel, and an oxidizer are required. In the case of a compartment fire the oxidizer is almost always O_2 present in air. The fuel can range from a hydrocarbon pool, to household furnishings. Heat is required to ignite the fuel.

Ignition can be initiated in two ways, piloted or non-piloted. Piloted ignition occurs when a high temperature source comes into contact with fuel. Non-piloted ignition occurs when fuel reaches a high temperature and spontaneously ignites when passing its Auto-Ignition Temperature (AIT), which is unique to every fuel [28]. After ignition, heat and smoke will be limited in this stage and the flame size will be small but growing.

Growth

1. Inadequate amount of fuel, fire enters decay phase
2. Inadequate amount of O_2, fire enters decay phase
3. Fire continues to flash-over and fully developed stage

If fuel and O_2 are not in short supplies, flashover will occur. Rapid flame spread occurs and unburned fuel will become involved in the fire due to the incident radiation from the hot gas layer.

Fully Developed After flash-over, the fully developed stage is reached. The entire fuel load is involved in the fire and the hot layer has descended to the floor. The compartment is at extremely elevated temperatures ($> 1000°C$) and is fatal to any occupants in the compartment [59]. Heavy flames and dark smoke, indicative of high amounts of soot, are present. Building elements may fail and the flames and gases escaping the compartment pose risks to neighbouring compartments or surroundings.

Decay Decay may happen after the growth phase if limited by fuel or O_2, or may happen after fully-developed conditions are reached. The room will start to cool in temperature as most of the fuel has been consumed. Solid elements still radiate heat and it is possible that a fire can re-initiate during this phase if O_2 is reintroduced to the compartment.

2.2 Fire Tests

Fire tests provide methods to characterize materials and to measure fire hazards. Fire tests help to understand fire and associated consequences. Data from tests can be used in fire models to develop empirical correlations which can be applied in design considerations.

They are instrumental in creating lower fire hazards in all types of industry and residential stuff. Standard fire tests provide universal guidelines for different testers and researchers to contribute to ideas and conclusions.

There are many standardized fire tests, of which the methodology is governed by organizations such as ASTM (American Society of Testing and Methods). These tests are publicly available and serve to help the insurance industry, fire code development, and builder and materials developers. These standards all relate to ignition, burning, and combustion characteristics of materials, in general focusing on building materials and furnishings. In general, fire tests can be classified in two ways - full-scale and small-scale. Full-scale tests are representative of real fire conditions, involving common fuel loads and realistic geometry. These tests are costly, time consuming, and have a certain amount of risk in performing them. Small-scale tests seek to provide fire safety knowledge on a reduced scale, that decreases the time, cost, and safety risk of full-scale tests, while still providing meaningful information. Small-scale tests are inherently not as representative for most real-world applications, but are applied to determine relative risks and can be combined with fire models to have predictive capabilities. In summary, small-scale tests are generally more versatile and cost-friendly, but full-scale tests are still necessary in some cases [39]. Two common tests which are relevant to this thesis work are the cone calorimeter test and the compartment fire test.

2.2.1 Cone Calorimeter

The cone calorimeter is a fire testing apparatus that measures the rates of heat release and mass loss of a specimen as it is exposed to a heat flux from a conically-wound electric resistance coil. This specimen is a small sample of the material under investigation, and the heat flux applied is high enough to initiate pyrolysis and combustion of the specimen. The purpose of the test is to determine the relative hazard a certain material could pose if exposed to fire conditions. For example, the amount of heat and combustion products a mattress would release when consumed by a fire. In addition to HRR and mass loss rate (MLR), total energy released, time to ignition, smoke production and gas concentrations are measured. A summary of the methodology is presented here, refer to ASTM E1354-16a for full details of the apparatus and standard operation of the test system [9].

The standard size of a specimen in the cone calorimeter test measures 100 mm $\times$ 100 mm in area, and up to 50 mm thick. Specimens are wrapped in aluminum foil and placed on a 13 mm thick layer of refractory fibre blanket inside a specimen holder constructed of 2.4 mm thick stainless steel with interior dimensions of 101.2 mm $\times$ 101.2 mm, and 22.6 mm deep.

Optionally, a steel retaining frame may be placed over the specimen, with stated the intent of reducing "unrepresentative edge burning of specimens" [9].

The heating element is wound into the shape of a truncated cone, with dimensions as indicated in Fig. 2.1. The outer shell of the heater is made of stainless steel, and a stainless steel radiation shield is positioned at the bottom of the heater to protect the specimen below from any heat exposure prior to the start of a test. Before a test is conducted, the cone heater is energized and its temperature increased to a user-specified setpoint; the cone heater is then allowed to stabilize for at least 10 min at the specified value. When the shield is opened, the specimen is exposed to irradiation from the cone heater and the test is initiated. Gases released from the specimen are collected and analyzed for species type and concentration. The HRR is determined from the principle of O_2 calorimetry, based on the fact that a correlation exists between the amount of O_2 consumed and the amount of heat released [9].

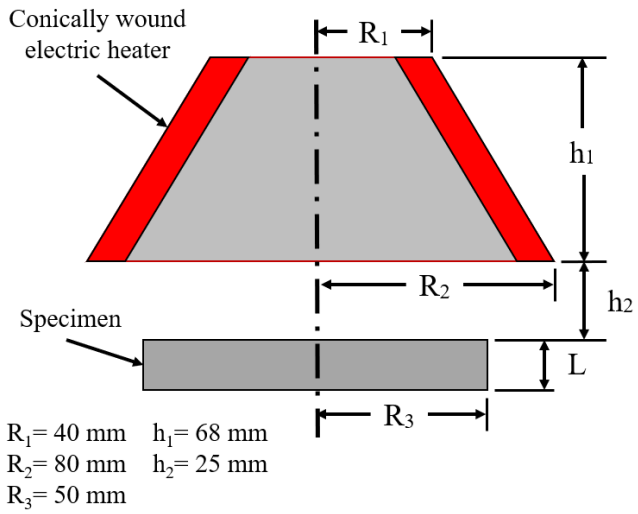

Figure 2.1: Schematic of the cone heater and specimen.

2.2.2 Compartment Fire Tests

As compartment fires are of primary importance especially in regards to residential homes, fire tests related to fire growth and wall construction within a compartment are standardized. ASTM E 119 was developed in 1905 after a large fire in Baltimore, and it was the first fire test standard adopted in 1918. This test uses a representative wall section and

exposes it to gas burners of a furnace. A prescribed temperature–time curve is applied and the temperature on the unexposed side measured. The failure criteria occurs for this test when any point reaches 180°C on the unexposed side or the average temperature reaches 140°C [8]. To determine the impact on wall and ceiling construction on the fire growth within a compartment, ASTM E 2257 was developed. In this test a compartment is built to specified dimensions, of 2.4 m × 3.6 m and has a single doorway [11]. Heat flux, HRR, species measurements, and the time to flashover are measured. Fire and flame spread are observed with special attention for the conditions leading to flashover. The test methodology can serve as a basis for compartment fire tests and provide researches with the ability to learn more about all aspects of fire by varying fuel loads and ventilation conditions. Many similar compartment fire tests have been performed, notably the Steckler fire tests, where 55 tests were conducted to study the fire conditions in the compartment and testing the predictions of fire-plume models [73].

2.3 Fire Models

Fire models are applied by fire protection engineers, researchers, building officials, and fire departments. As the safety cost and fire risk of performing experimental tests is high, fire modelling can be used in conjunction with or as an alternative to experiments for characterizing materials, design purposes, and fire investigations, amongst others. Fire models are implemented in locations where objective based fire codes are implemented, as a tool that can prove a building can meet the requisite amount of fire protection [56]. While fire modelling has progressed significantly in the past few decades, there are still many phenomena related to fire that are difficult to model. Flashover, pyrolysis, and degrading materials are three areas that pose these modelling challenges. Flashover is challenging due to the instantaneous nature of the phenomena and the vast changes of the compartment that occur as a result. Pyrolysis and degrading materials are hard to model due to the complex interaction of heat and mass transfer, and changes in material properties that occur during burning.

There are several classifications of fire models available, each suited for different purposes. These can include hazard models, risk models, and egress models [40, 79]. Depending upon the application the appropriate model to use is based upon factors such as cost, accuracy, user knowledge, and level of detail required. Fire models can be classified in three ways - algebraic, zone models, and field models. Algebraic models are mathematical expressions or engineering correlations that are based on experimental observations, and therefore empirical in nature. These are useful for design work and estimations. They

can provide rough estimates that are applicable in limited scenarios and are generated by applying significant amounts of assumptions. For example, calculating the smoke layer in a room can be estimated based upon the room dimensions, HRR, and time elapsed since ignition [28].

Zone models use a control volume approach, applying simplified governing equations for mass and energy along with engineering correlations. Generally a room is split into two zones, a hot layer zone and a cold layer zone. The cold layer is air at ambient conditions, while the hot layer is at elevated temperatures and be representative of combustion gases, and smoke production. The height of the interface between zones will change throughout the simulation. As the fire progress the hot layer would increase in size, descending from the ceiling. Mixing is calculated between zones through an energy balance. The goal of zone models is to look at smoke and heat transfer and are used in practical engineering applications due to their history of reliability in limited capabilities. These models are more complex than algebraic models and generally need specialized software. Common examples of zone models include CFAST [55] and OZone [19]. Zone models are appropriate for simple to moderate scenarios at a relatively small computational cost. However, they produce limited information about the fire environment and still rely on many assumptions. Zone models are not well suited to complex fire situations or for predictive modelling capabilities.

Field models, also called CFD models are an extension of zone models which split a domain into a large number of zones (cells). The complete governing equations for mass, momentum, energy, and species transport are solved and the velocity and pressure field is determined at each cell [80]. Field models incorporate a more detailed amount of physics compared to zone models and algebraic models. In addition, fields models allows a wider range of physics to be accounted for such as pyrolysis, combustion, turbulence, radiation etc. Field models can accommodate these physical phenomena by implementing sub-models, whereas zone models cannot due to the lack of solving for a velocity field [37]. For complex phenomena such as fire, this allows a more accurate reflecting of the flow dynamics, while applying fewer assumptions. Field models can have a significant variation in modelling capability and input requirements. Specialized fire codes include combustion and pyrolysis models and model the chemical effects of the fire, whereas general field models rely on a higher amount of prescribed inputs, such as specification of a HRR. This is a greatly simplified approach and assumes that the HRR over time data is available, which is often not the case. Some field models include heat transfer through walls, however an assumption of one-dimensional conduction is prevalent. This assumption neglects the nature of most walls, which have multi-dimensional heat transfer due to the geometry of structural elements. In general, field models are applied when a high degree of accuracy is required, or when predictive capabilities are required.

2.3.1 Computational Fluid Dynamics (CFD)

Since CFD is the focus of the thesis, the general CFD technique will be outlined here. The approach is termed the finite volume method due to the solving of governing equations over discrete control volumes. The purpose is to solve a physical problem involving fluid flow with a high degree of accuracy and generate informative results. This is accomplished through the following six steps:

1. Definition of computational domain
2. Domain discretization (meshing)
3. Selection of numerical approach
4. Prescribe initial and boundary conditions
5. Solution
6. Post-processing

The geometry of interest is selected and either generated with the assistance of computer aided design (CAD) or with a CFD solvers' proprietary geometry program. The dimensions of the domain to be modelled are inputted and the user decides the extent of the domain to model. For example, in a compartment fire test, will only the compartment itself be modelled or will the domain be extended to contain a certain amount of the external environment around the compartment as well.

Once the geometry is defined, it must be discretized. This domain is split into a large number of finite cells to create a "mesh". There are multiple ways to do this and it is up to the user to apply appropriate sizing and refinement in areas of interest and high gradients in velocity and pressure. Since the cells are refined to small sizes, the properties of each cell can be considered uniform. However, it is important to ensure the mesh is refined enough for this to be true. A grid independence check is always necessary. Cells that are too large introduce errors into the solution as the assumption of uniform properties does not hold [80].

Before the governing equations are solved on each cell, the selection of the appropriate physics is made. Common models across all fire solvers are turbulence, combustion, and radiation. The turbulence model is important as it forms the basis of the CFD approach, to calculate the velocity and pressure fields. Combustion has many approaches available based upon amount of detail in the chemistry and numerous assumptions. Radiation has

multiple models available depending upon the accuracy required and how large a role radiation is expected to play in the scenario. Numeric schemes are set to determine the accuracy required of the solution.

Initial and boundary conditions are specified to provide a starting point for the computations. Ambient conditions are usually applied as the initial conditions for transient simulations. Openings are defined at boundaries that are open to the environment. The solver can calculate the direction of flow and associated properties at these boundaries. Finally, the fire source is commonly defined as a MLR or HRR boundary condition.

Before running the solution, suitable convergence criteria and iteration size are set. Setting an appropriate iteration interval for steady state, or a time interval for transient flows, is critical to ensure accurate results without using unnecessary computation time. To reduce the computational time, parallel computing is optional. Parallel computing splits the computational domain into a number of subdomains; each subdomain is run on a separate processor for significantly faster simulation time. This technique can be performed locally on one machine or group of machines or run on a cluster of super-computers. In this thesis work the supercomputer cluster SciNet, based out of the University of Toronto is utilized.

Finally, results are generated in the form of data file for pressure, velocity, temperature, etc. These results can be visualized in post-processing tools, or exported to a software such as MATLAB to tabulate and graph. Calculations are sometimes required based upon the desired output parameters. For example, if a flow rate is required, velocity needs to be summed through the geometry of interest.

2.3.2 Fire Solvers

Many commercial CFD models do have some extent of fire functionality such as ANSYS Fluent [7], ANSYS CFX [6], and Star CCM+ [67]. However, there are dedicated solvers formulated specifically for fire scenarios. Two of these most prevalent fire models are FireFOAM [32] and Fire Dynamics Simulator (FDS) [52]. FireFOAM is based upon the OpenFOAM package which is an C++ driven code. This code is developed by FM Global and permits access and customization to the source code. This access allows researchers to implement custom sub-models and improve built-in capabilities. FDS is developed by the National Institute of Standards and Technology (NIST). FDS allows only rectilinear coordinates, which means complex shapes can't be accurately modelled. Both these models are formulated for low Mach number flow ($< 0.3\times$ speed of sound), which is typical of fire type scenarios. This eliminates compressibility effects which are present at high speed

flows and allows the governing equations to be simplified. Both models primarily solve the gas phase dynamics and then add sub-models to account for combustion, radiation, water suppression, and pyrolysis. FDS is more commonly applied in industrial applications whereas FireFOAM is more commonly selected for research purposes. As reviewed by Trouvé and Wang [77], the majority of models developed using these platforms employ similar approaches to turbulence, combustion, and radiation modelling, a one equation turbulent kinetic energy sub-grid scale (SGS) approach, eddy dissipation concept (EDC) with one-step complete combustion, and a simplified form of the radiative transport equation (RTE), respectively. In a study of reduced scale under-ventilated C_7H_{16} fueled compartment fires, Vilfayeau et al. [81] develop a flame extinction model within fireFOAM and implement an EDC approach for turbulence, with a one equation eddy viscosity model, and a modified reaction mechanism. Reasonable agreement is found with temperature and MLR experimental measurements. However, CO is not modelled and no species comparisons are presented. Cai and Chow [20] modelled the HRR within a compartment using FDS. Different ventilation amounts were investigated by varying the height of the single doorway into the compartment. Poor predictions were found when using the liquid fuel model within FDS. A series of experimental tests were performed by Andrews et al. [5] in a reduced scale compartment which focused on the products of incomplete combustion including CO and NO_x. Ventilation amounts equal to three leakage rates were tested to simulate an enclosed room. Significant CO production, along with a corresponding depletion of O_2, was found in the case where the fire had a sufficient amount of ventilation to develop. Hosser and Hohm [37] developed a model within FDS to account for heat transfer to solid surfaces in the case of full-scale fire tests. The model performed well and was an improvement over the unmodified version of FDS. In summary, fire modelling is an evolving area of research working towards reducing the amount of simplifications present in CFD simulations.

Chapter 3

Thermal Modelling of Cone Calorimeter Tests

This chapter outlines the preliminary work done on modelling heat transfer of the cone calorimeter test. The experimental approach on which the modelling is based is detailed. Two numerical approaches are developed, one that is a finite difference approach implemented in MATLAB. The second is a CFD formulation implemented in OpenFOAM. In addition to providing predictive capabilities, the CFD case is a first step in developing a more complex formulation based upon full-scale fire experiments.

3.1 Experimental Set-up

The experimental set-up differs from the standardized cone calorimeter test. In the standard test, there are limitations in the understanding and control of the experimental conditions encountered by a specimen which provide challenges for problem definition and accompanying model formulation.

In the experimental characterization, one issue is related to the positioning of an instrumented specimen under the cone heater, which is typically pre-heated to temperatures in excess of 500°C, before a standard test. The specimen must be positioned carefully on the load cell, accounting for the additional instrumentation, in a sufficiently short amount of time so as to avoid pre-heating of the specimen through the cone heater radiation shield. Any adjustments that might need to be made to the instrumented specimen are difficult to

make due to the close proximity to the hot cone heater (e.g. adjusting the spacing between the specimen and cone heater).

The standard test is idealized as 1D heat transfer through the depth of the specimen. However, this is not the case due to two reasons. Firstly, the heat flux exposure is non-uniform across the surface of the specimen. Secondly, heat transfer occurs at the sides of the specimen — radiative exchange between the specimen sides, cone heater, and surroundings, as well as convective cooling. ASTM E1354-16a specifies that heat flux measured within a central 50 × 50 mm region below the heater should be within ±2% of the centreline value [9]. Choi [24] investigated the three-dimensional temperature gradient that developed within ceramic fibreboard instrumented with thermocouples under various constant heat flux exposures and found this to be true for centreline heat flux values ranging from 10 to 80 $\mathrm{kWm^{-2}}$, although he noted that the heat flux at the corners of a standard-sized specimen (100 mm × 100 mm) was approximately 30–40% less than the centreline value. This is primarily caused by the non-uniformity of irradiance over the exposed specimen surface. This finding is in agreement with that of Boulet et al. [17], as measured using IR thermography, as well as that of Wilson et al. [86], Gemaque and Costa [33], and Kang et al. [41]. From these studies it is well known that irradiance is at a maximum in the central region of the specimen, decreasing radially outward from $r = 0$, as shown in Fig. 3.1. To

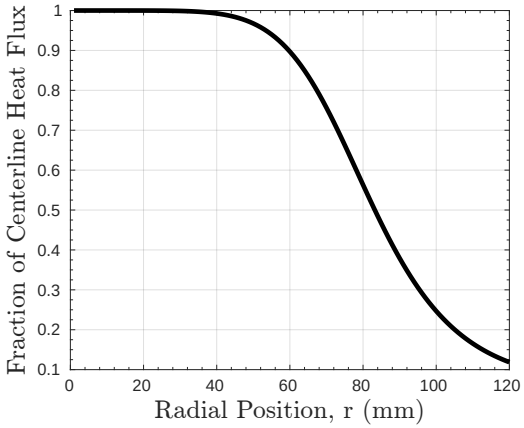

Figure 3.1: Fraction of maximum (centreline) heat flux at increasing radial positions of a cylindrical specimen [86].

address both the experimental and modelling concerns a modified experimental approach is proposed which uses a transient heat flux exposure, and a large radial specimen with uninsulated sides.

A cylindrical specimen is prepared from nominally 6.35 mm (1/4 inch) hot-rolled A36 steel plate to a diameter of 224 mm. Given that irradiance is dependent on the spacing between the cone heater and specimen, a thick plate is selected to avoid the occurrence of warping as the plate is heated. The specimen surfaces are ground and polished to remove scale and any trace oil, reducing the final thickness to 6.20 mm. The top and side surfaces of the plate are then coated in matte black VHT $Flameproof^{TM}$ paint. Three 24 gauge K-type glass fibre sheathed thermocouples are welded directly to the bottom surface of the specimen at radial positions of 0 mm, 70 mm, and 100 mm. The steel specimen is placed on three layers of Fiberfrax® Durablanket® S refractory ceramic fibre blanket with nominal density of 128 kg/m^3 (8 lb/ft^3) and thickness of 25.4 mm (1 inch) per layer. Bead-welded exposed junction thermocouples (of the same type as above) are placed between each insulation layer and at the bottom of the insulation at the centreline. A single layer of 10.6 mm thick HardieBacker® cement board is placed under the insulation; this layer simply adds rigidity to the assembly, since it is not expected to undergo significant heating through the thick insulation layer. With the insulation compressed between the steel plate and cement board the thickness is reduced to 56.0 mm. The instrumented specimen assembly is placed on the load cell in a position coaxial with the cone heater, with a separation distance of 25 mm. Mass data is not recorded, since the steel plate does not degrade. Figure 3.2 shows the specimen assembly schematically along with the instrumentation described above. Two transient exposures are applied. Ramp25 and Ramp50 apply an irradiance starting at 0 and exponentially grow to 25 kW/m^2 and 50 kW/m^2, respectively.

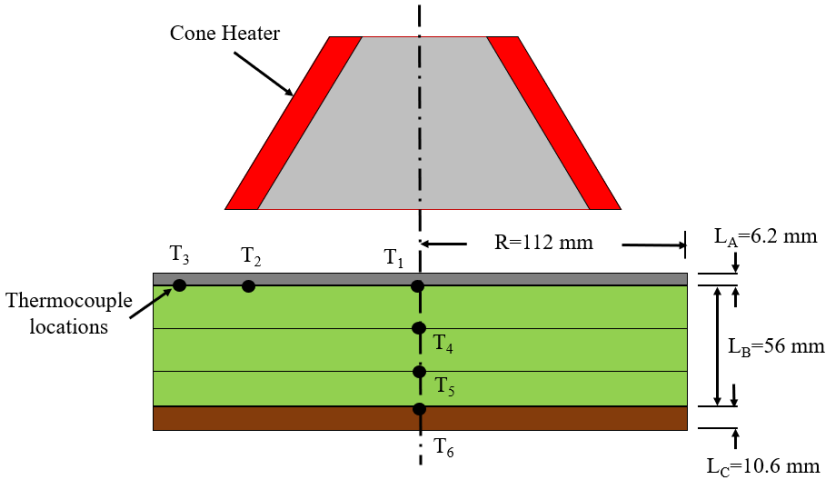

Figure 3.2: Schematic of the instrumented specimen assembly.

3.2 Finite Difference Model

A finite difference model is a discretized model of equations that allows for numerical implementation. This model is developed with the goal of predicting the temperature profile within a specimen exposed to irradiance from a cone calorimeter. Two versions are created, both a one-dimensional (1D) and two-dimensional (2D) axisymmetric model for the experimental procedure outlined in Section 3.1.

A range of models have been developed in the past with varying degrees of complexity. One model is created by Aire during his MASc thesis [4]. It uses a 1D finite difference scheme to solve for temperature at nodal locations throughout different wall assemblies. Typically, these wall assemblies consist of one or two layers of gypsum board and insulation. Bulk properties for gypsum board, make use of the "apparent heat capacity" method. This method implicitly models the phase change and is a simplification to reduce the modelling complexity. By using the bulk properties of wood and gypsum board complex phase effects such as the vaporization of the entrained water can be modeled without a significant increase in computational cost. This is a common approach amongst finite difference models [4, 34, 76, 83]. An example of this is the Eurocode treatment of wood decomposition: a 3D conduction model simply predicts the temperature evolution within the solid material, and thermal decomposition is represented implicitly by temperature dependent material properties [29]. More complex models such as CU Woodframe, a

model developed by Craft, apply a finite element approach to capture 2D effects and include complex processes such as moisture movement and degradation of materials, which is beyond the scope of what is done in MATLAB [25, 26]. While degrading specimens are not looked at in the current work, some generalized models of pyrolysis, such Gpyro3D [45] and Thermakin2D [74], can be applied to multidimensional problems, but in most cases a 1D model, such as Gpyro [46], ThermaKin [75], or Pyropolis [70], is used for study of the pyrolysis of cone calorimeter specimens. This simplification is justified on the basis of a presumed uniform thermal gradient within the specimen, which may not actually be the case, as demonstrated.

3.2.1 Formulation

A time explicit finite difference scheme is derived using the energy balance method for both 1D and 2D formulations [14]. The governing equation to be solved in this heat transfer problem is conservation of energy combined with the constitutive relationship of Fourier's Law of Conduction. The resultant form is shown in Eq. 3.1 for a one-dimensional (1D) model formulation and Eq. 3.2 for a two-dimensional axisymmetric (2D) formulation, given by

$$\rho c_p \frac{\partial T}{\partial t} = \frac{\partial}{\partial z}\left(k \frac{\partial T}{\partial z}\right); \tag{3.1}$$

$$\rho c_p \frac{\partial T}{\partial t} = \frac{1}{r}\frac{\partial}{\partial r}\left(kr \frac{\partial T}{\partial r}\right) + \frac{\partial}{\partial z}\left(k \frac{\partial T}{\partial z}\right). \tag{3.2}$$

First-order finite difference approximations are applied to the spatial derivatives at the boundary nodes and temporal derivatives, while second-order finite difference approximations are applied at the interior nodes. The surface nodes are made half as thick to improve accuracy of the solution. Multiple layers are modeled. Therefore, special attention is made for the derivation of the interface nodes between surfaces. The materials are referred to in the order they positioned below the cone heater. Therefore, material 'A' is steel, material 'B' is insulation, and material 'C' is cement board. The governing equations are discretized over the model domain which is the solid specimen to be modeled. The effect of the surroundings, including the cone heater and ambient air are taken into account using boundary conditions. Finally, transitional boundary conditions between each material layer are coupled (contact resistance is neglected).

3.2.2 Boundary Conditions

In these models, only the specimen itself is modeled. The ambient, surroundings, and cone heater are resolved into boundary conditions. The steel supporting rod which holds the specimen is assumed to have a negligible impact on the temperature profiles as it is attached to the unexposed surface where the temperatures are very close to ambient. Initially, it is assumed that the temperature of all materials is equal to the ambient temperature T_∞. The heat transfer boundary conditions on the surfaces of a cone calorimeter specimen can be categorized by the modes of heat transport at a given surface: radiative, convective, and conductive. The primary source of heat transport in to the specimen is the cone heater irradiation.

Exposed surface

On the exposed side there is radiation from the cone heater to the specimen surface. The cone heater coil is assumed to be an ideal or black body emitter ($\varepsilon = 1$) as has been proven to be a negligible difference from its actual emittance [16, 17]. There is convection and radiation from the specimen's surface to the ambient and surroundings. The boundary condition on the exposed surface (top) of the steel plate (A) is given by

$$\left.\frac{\partial T}{\partial z}\right|_{z=0} = \frac{\varepsilon_A}{k_A} q_e'' - \frac{\varepsilon_A \sigma}{k_A}\left(T_s^4 - T_\infty^4\right) - \frac{h_{c,top}}{k_A}\left(T_s - T_g\right), \tag{3.3}$$

where q_e'' is radiative heat flux from the cone. As q_e'' is the needed input to the model, a calibration curve is developed to relate q_e'' and T_c^* using a Schmidt-Boelter heat flux gauge positioned 25 mm below the cone heater at $r = 0$. This curve is shown in Fig. 3.3. From Fig. 3.3, two setpoint values of T_c^* are selected: 575°C corresponding to 25 kWm^{-2}, and 754°C corresponding to 50 kWm^{-2}. The transient "Ramp25" and "Ramp50" exposures are then recorded by energizing the cone heater from an initially cold state using the above setpoint values. For these tests the standard heat flux gauge and cone heater thermocouples measure q_e'' and T_{cone}. A thermocouple is positioned adjacent to the heat flux gauge to measure the hot gas temperature (T_g) near the centreline. The characterized centreline exposure profiles are shown in Fig. 3.4 along with the measured hot gas temperatures. With the transient centreline exposures profiled, the next step is to characterize the spatial dependence of incident heat flux. Two additional tests are conducted using the same cone heater temperature setpoints as above. Results for both experiments are shown in Fig. 3.5. The figure demonstrates that the irradiance in the central region is quite uniform, but

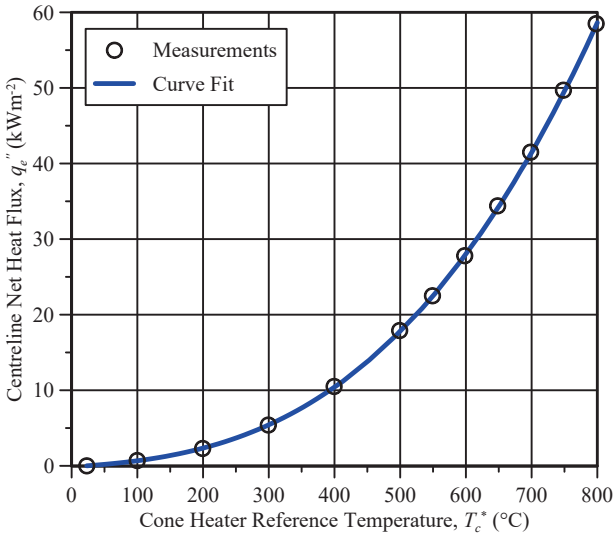

Figure 3.3: Calibration curve for the relationship between q_e'' and T_c^*.

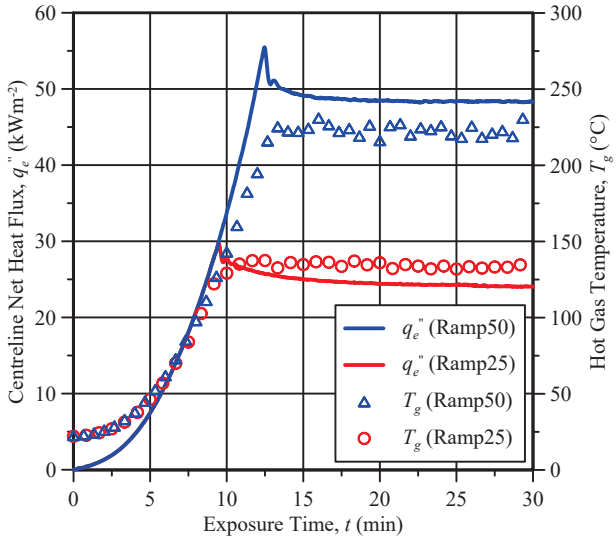

Figure 3.4: Transient centreline exposures and hot gas temperatures.

beyond 35 mm from the centreline the irradiance decreases. For the 1D model formulation, N_{tot} is used in the computation of q_e''; N_{tot} is calculated from $N(r)$ by area integral similar

to a total view factor:

$$N_{tot} = \frac{2}{R^2} \int_0^R N(r) \cdot r dr, \tag{3.4}$$

resulting in a value of 0.5940 for a specimen with radius of 112 mm. This is a simplification necessary due to the 1D nature of the formulation; the reality is that the measured centreline heat flux from the conical heater to a specimen is not uniform over the entirety of its surface. To account for this non-uniformity, a normalization function $N(r)$ is defined such that

$$q''_e(r,t) = N(r) \cdot q''_e(r,t)|_{r=0}. \tag{3.5}$$

The centreline-normalized heat flux N is then computed using Eq. 3.5 for each heat flux measurement, and mean values of N are calculated based on the measurements at each radial position. As shown in Fig. 3.5, the results are essentially identical for both tests. A non-linear curve fit is applied to the mean values of N

$$N(r) = d + \frac{a-d}{1+(r/c)^b}, \tag{3.6}$$

where: $a = 1.000$, $b = 6.774$, $c = 81.86$, $d = 0.05262$, and the coefficient of determination is 0.9997. The normalization function is then compared to the theoretical centreline-normalized view factor, $F_{\mathrm{d1,3}}(r) / F_{\mathrm{d1,3}}(r)|_{r=0}$, which is analogous in concept. Figure 3.5 demonstrates that the measured irradiance decreases less at large radial positions than would be expected based on the view factor for a simplified cone geometry. Finally, the experimentally-characterized $q''_e(r,t)$ is computed for both Ramp25 and Ramp50 exposures as the product of $N(r)$ and $q''_e(r,t)|_{r=0}$.

Unexposed surface

The boundary condition on the unexposed (bottom) surface of the cement board (C) is given by

$$\left.\frac{\partial T}{\partial z}\right|_{z=L} = -\frac{\varepsilon_C \sigma}{k_C}\left(T_s^4 - T_\infty^4\right) - \frac{h_{c,bot}}{k_C}\left(T_s - T_\infty\right). \tag{3.7}$$

Eq. 3.7 assumes that the bottom surface is completely open — contact with the load cell platform is neglected. This is a reasonable assumption due to the low amount of heat transfer through the load cell, due to the low temperatures expected on the bottom of the specimen.

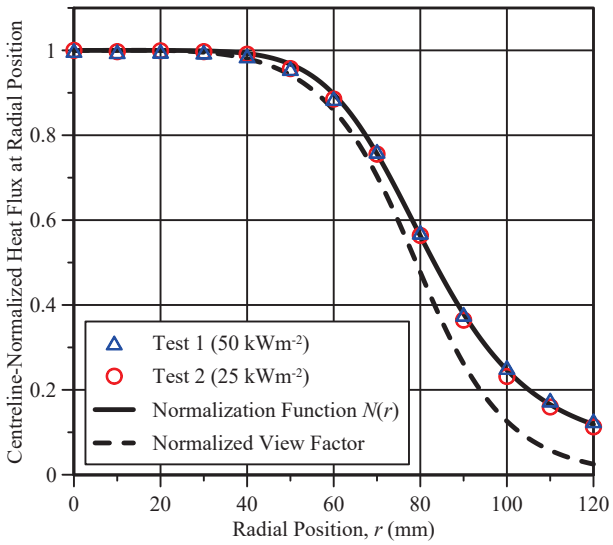

Figure 3.5: Experimentally-determined normalization function $N(r)$ in comparison to the centreline-normalized differential view factor $F_{\mathrm{d1,3}}(r)/F_{\mathrm{d1,3}}(0)$.

Side surface

The boundary conditions on the side surfaces of the steel, insulation, and cement board take a similar form

$$\left.\frac{\partial T}{\partial r}\right|_{r=R} = -\frac{\varepsilon_i \sigma}{k_i}\left(T_s^4 - T_\infty^4\right) - \frac{h_{c,side}}{k_i}\left(T_s - T_\infty\right), \tag{3.8}$$

where i represents the material (A, B, or C).

The sides of every layer are exposed to the ambient and surroundings. Again, the surroundings and ambient are assumed to be at the same temperature. The emissivity and convection coefficient depend on the material properties and physical dimensions of each layer, respectively.

Convection heat losses

The convection heat transfer coefficients are all calculated according to a similar procedure outlined here. A constant value of h_c is often assumed at the top surface in models; Ryder [62] reported that most studies use values between 10 and 20 $\mathrm{Wm^{-2}K^{-1}}$, although values spanning from 7 to 34 $\mathrm{Wm^{-2}K^{-1}}$ have been used in some cases. However, it is well recognized that h_c depends on both the temperatures of the solid and the gas, as well as

the gas velocity in the case of forced convection. Since the gas velocity adjacent to a cone calorimeter specimen tends to be small, a natural convection model is often adopted, as done by Staggs [71, 72]. Additionally, it was demonstrated by Lam [44] that q_{conv} is more accurately calculated using the local gas temperature adjacent to the specimen (T_g) rather than the "ambient" value of T_∞.

Convection heat transfer is modelled on all three surfaces using correlations for natural convection external flow [14]. For each surface i, the mean Nusselt number ($\overline{\mathrm{Nu}_L}$) is calculated from the Rayleigh number (Ra_L), which depends on the mean temperature over the characteristic length of the surface (T_s) and the gas temperature near to the surface (T_g)

$$\mathrm{Ra}_L = \frac{g\beta(T_s - T_g)L^3}{\nu\alpha}, \tag{3.9}$$

where g is standard gravity (ms^{-2}), ν is the kinematic viscosity of the gas ($\mathrm{m}^2\mathrm{s}^{-1}$), α is the thermal diffusivity of the gas ($\mathrm{m}^2\mathrm{s}^{-1}$), L is the characteristic length of the surface (m), $\beta = 1/T_f$, and $T_f = (T_s + T_g)/2$ (K) is the film temperature. The average convective heat transfer coefficient is then calculated from Eq. 3.10 for each surface i

$$h_{c,i} \approx \frac{k\overline{\mathrm{Nu}_L}}{L}, \tag{3.10}$$

where k is the thermal conductivity of the gas ($\mathrm{Wm}^{-1}\mathrm{K}^{-1}$). All gas properties are evaluated from those of air at T_f.

The characteristic length of the top surface of the specimen is taken to be the area divided by the circumference ($D/4$), and Nusselt number is calculated as follows [14]

$$\overline{\mathrm{Nu}_L} = \begin{cases} 0.54\mathrm{Ra}_L^{1/4} & 10^4 < \mathrm{Ra}_L < 10^7; \\ 0.15\mathrm{Ra}_L^{1/3} & 10^7 < \mathrm{Ra}_L < 10^{11}. \end{cases} \tag{3.11}$$

Similarly, Nusselt number for the bottom surface of the cement board is calculated as follows [14]

$$\overline{\mathrm{Nu}_L} = \Big\{ 0.27\mathrm{Ra}_L^{1/4} \quad 10^5 < \mathrm{Ra}_L < 10^{10}. \tag{3.12}$$

The convection heat transfer coefficient for the side surface of the specimen assembly is calculated using a correlation for external flow around a vertical cylinder. Assuming that all three materials form a single continuous isothermal surface at mean temperature T_s, a continuous boundary layer will form along the sides of the assembly with a characteristic

length equal to the total thickness. If the criterion for the "thick cylinder limit" ($D/L > \mathrm{Ra}_L^{-1/4}$) is satisfied, then the Nusselt number is calculated as follows [14]

$$\overline{\mathrm{Nu}_L} = 0.68 + \frac{0.67\mathrm{Ra}_L^{1/4}}{[1 + (0.492/\mathrm{Pr})^{9/16}]^{4/9}}, \tag{3.13}$$

otherwise, the following expression [48] is applied

$$\overline{\mathrm{Nu}_L} = \frac{4}{3}\left[\frac{7\mathrm{Ra}_L\mathrm{Pr}}{5(20 + 21\mathrm{Pr})}\right]^{1/4} + \frac{4(272 + 315\mathrm{Pr})L}{35(64 + 63\mathrm{Pr})D}, \tag{3.14}$$

where Pr is the Prandtl number evaluated at T_f.

Given the bounds of Eqs. 3.11–3.14, a value of 2 $\mathrm{Wm}^{-2}\mathrm{K}^{-1}$ is set as the lower limit for h_c. This is not expected to have a notable impact on model results, since a small value of h_c would correspond to a small value of T_s, in which case q_{conv} would be small regardless of the value of h_c. Figure 3.6 shows the values of h_c used in the present study for each surface plotted as a function of surface temperature assuming that $T_g = T_\infty$. The convective heat transfer coefficient for the top surface is slightly greater than that from Zhang and Delichatsios [89], and approximately 50% less than that from Staggs [72].

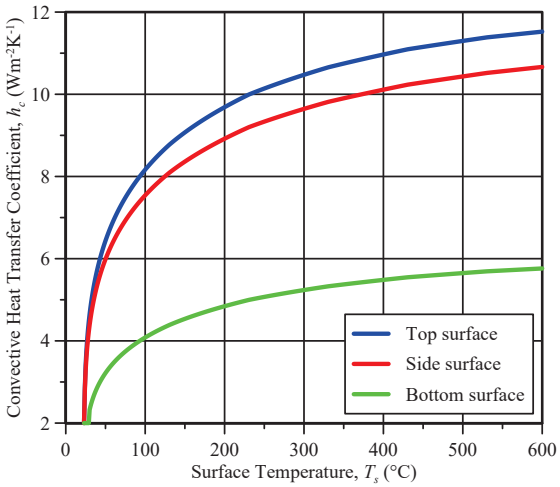

Figure 3.6: Temperature-dependent convective heat transfer coefficients.

3.2.3 Thermophysical Properties

Most wall materials, such as gypsum board and wood, have temperature dependent thermophysical properties [13]. While not required for the non-degrading materials presented here, this model accommodates analytical expressions for these properties. For example, the material properties of a spruce specimen are shown in Figs. 3.7–3.9. There are represented by a curve fit that allows for a polynomial representation to be inputted to the model. Of interest is the spike in the specific heat graph which indicated the endothermic reaction of water vaporization at approximately 373 K. This approach would make use of the "apparent heat capacity" to implicitly model the complex phase change effects of materials without increasing the computational cost. Thermophysical properties of the materials

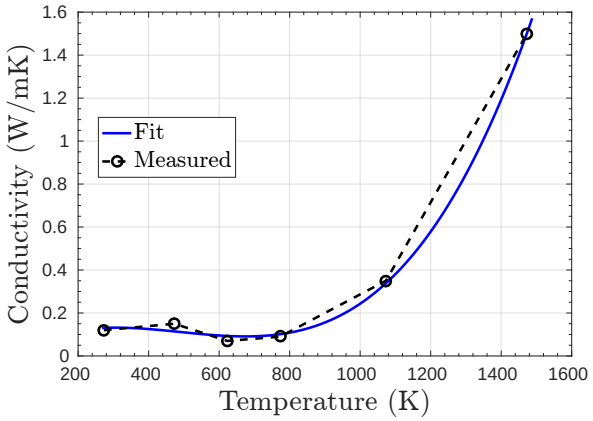

Figure 3.7: Conductivity of spruce.

in this study are obtained from various external sources, and are listed in Table 3.1. Steel properties are adopted from Zhang and Delichatsios [89], who conducted a similar study of heat conduction for a steel plate under cone calorimeter exposure. Insulation properties are obtained from the manufacturer [3, 61], and the expression for thermal conductivity is developed from the tabulated data. Note that the insulation is compressed by approximately 25% in this application; no data was available for the thermal conductivity or specific heat capacity of the insulation in its compressed state. Properties are available for a similar material compressed to 25%, Thermal Ceramics Cerablanket® [10], which has the same nominal density and thickness as the insulation used here. These properties are comparable to the properties in Table 3.1 for Fiberfrax®. Cement board properties are

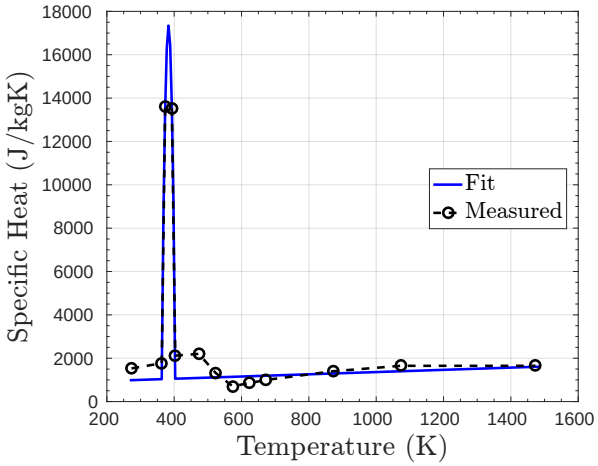

Figure 3.8: Specific heat of spruce.

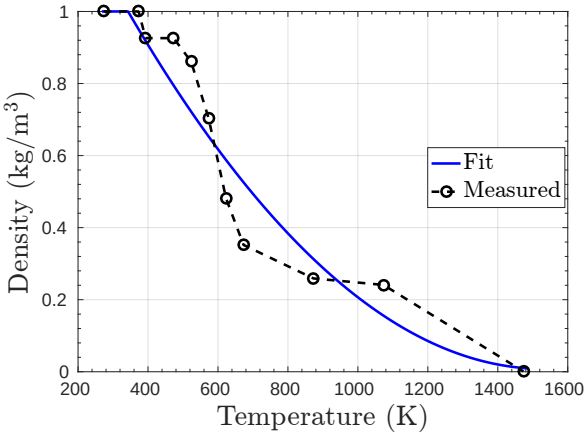

Figure 3.9: Density of spruce.

taken from previous work done with the material at the University of Waterloo [2, 43]. Apparent emissivity $\varepsilon(T_s)$ of the painted steel plate is determined experimentally, using a hot plate and infra-red (IR) camera to measure the temperature dependent values. A non-linear curve fit is applied as seen in Eq. 3.15.

$$\varepsilon(T_s) = d + \frac{a-d}{1+(T_s/c)^b}, \tag{3.15}$$

where: $a = 0.9339$, $b = 2.902$, $c = 342.2$, $d = 0.9916$, and the coefficient of determination is 0.9928. As opposed to the top surface of the cylindrical steel plate, the side surface is roughly cut, unpolished, and only partially coated by paint. Since the radiative properties of this surface are unknown, and expected to differ significantly from those of the top surface, emissivity is estimated to be 0.75 [14].

Table 3.1: Thermophysical properties of the materials comprising the multi-layer specimen (T has units of Kelvin).

Property	Steel (A)	Insulation (B)	Cement Board (C)
k ($\mathrm{Wm^{-1}K^{-1}}$)	42	$0.01389e^{0.002375T}$	0.227
ρ ($\mathrm{kgm^{-3}}$)	$7850/\left(1+0.004\left[\left(T-273.15\right)/1000\right]^6\right)$	94.18	1150
c_p ($\mathrm{Jkg^{-1}K^{-1}}$)	$486.522 + 161.044T/1000 + 418.014(T/1000)^2$	1130	1090
ε	Eq. 3.15	0.85	0.54

3.2.4 Degradation

Although the current multi-layer specimen is non-degrading at the temperatures investigated, it is important to allow some degree of pyrolysis modelling capability in the model. A simple pyrolysis model is optional for the purposes of predicting mass loss and the formation of char. The model uses a critical temperature to determine the transition from wood to char. Wood and char have different values of bulk properties (k, ρ, C_p) to account for the degradation of the specimen. In addition, different radiation properties (ϵ_{wood},α_{wood}, ϵ_{char}, α_{char}) are applied. This is a simplistic approach, and if pyrolysis becomes of interest in the future a more detailed pyrolysis model should be implemented. Sinha [69] reviews a number of methods on how to model pyrolysis, including multi-step reactions and modelling individual components of wood, and compares a simple decomposition mechanism (3 steps) to a more complex mechanism (5 steps), as proposed by Fateh et. al [30].

3.2.5 Numerical Sensitivity

A numerical stability check is made at each time step to ensure convergence of the solution. In the present study, the temperature of the surface node must always be greater or equal to the temperature at the previous time step during the heat exposure [14]. If the stability check fails, a warning is displayed and the time step needs to be decreased. A time step of 0.04 s is found to be sufficiently small. For the 1D model, Δz is taken to be 1.24 mm for material A, 4.67 mm for material B, and 2.12 mm for material C. For the 2D model, Δz is taken to be 1.24 mm for material A, 1.87 mm for material B, and 1.77 mm for material C; Δr is taken to be 3.2 mm. The numerical predictions are found to be grid independent. A 1D model has been first created which converges to the closed-form solution for the steady state problem when using a uniform and constant irradiance. When neglecting heat losses from the side surfaces the 2D model produced results that are almost identical to the 1D model.

3.2.6 Results

Experimental results for the Ramp25 and Ramp50 tests are presented below along with the 1D and 2D model predictions. As shown in Fig. 3.2, T_1, T_2, and T_3 refer to the thermocouple positions on the bottom of the steel plate at radial positions of $r = 0$ mm, $r = 70$ mm, and $r = 100$ mm, respectively. Similarly, T_4, T_5, and T_6 refer to the thermocouple positions in the insulation, at the centreline, at depths of 18.7 mm, 33.3 mm, and 56.0 mm below the bottom of the steel plate, respectively.

Ramp25 Exposure

Figure 3.10 shows results for temperature at the bottom of the steel plate. Steady state steel temperatures are observed after approximately 60 min of exposure. After 90 min, the temperatures measured are 416°C at T_1, 385°C at T_2, and 360°C at T_3. The temperature differences are not large between these radial locations due to the high thermal conductivity of steel. The 2D model predictions compare well with measurements. In the worst case, the 2D model under-predicts by 7°C at T_3. The average steel temperature is 376°C for the 2D model, calculated using an area integral, compared to 399°C for the 1D model (an over-prediction). The centreline temperatures through the depth of the insulation are shown in Fig. 3.11. After 90 min, the temperatures measured are 297°C at T_4, 184°C at T_5, and 55°C at T_6. Both models significantly under-predict the insulation temperatures, with the 2D model's results in slightly better agreement. In the worst case, both models

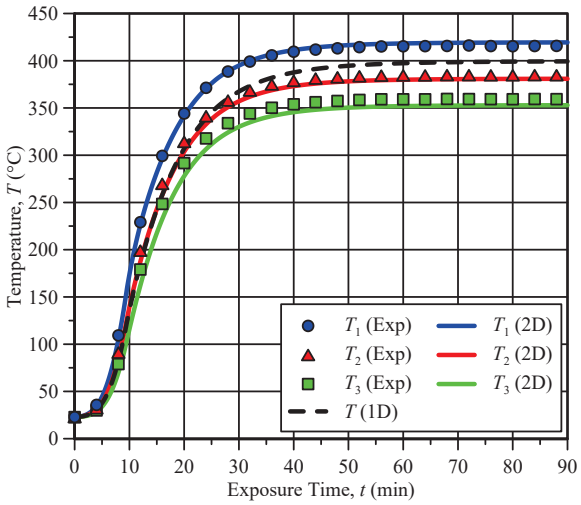

Figure 3.10: Steel plate temperatures for the Ramp25 exposure.

under-predict the insulation temperature by 23°C at T_5. Notably, the 2D model has a much better transient response than the 1D model, as evidenced by the results for T_4.

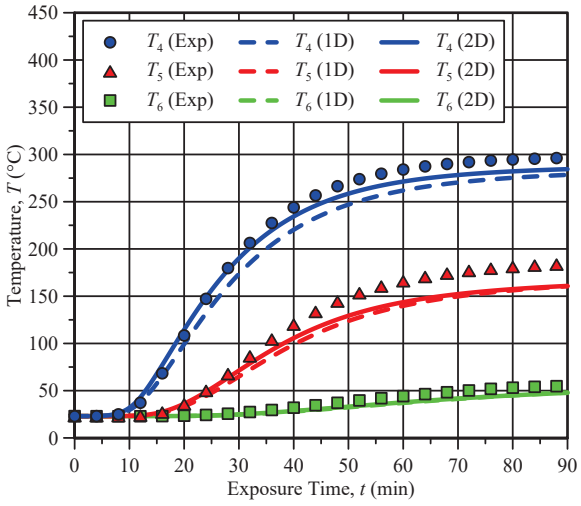

Figure 3.11: Insulation temperatures for the Ramp25 exposure.

Ramp50 Exposure

Temperatures at the bottom of the steel plate are well predicted for the Ramp50 exposure, as seen in Fig. 3.12. After 90 min, the temperatures measured are 598°C at T_1, 538°C at T_2, and 487°C at T_3. In the worst case, the 2D model under-predicts the temperature by 13°C at T_3. The average steel temperature is 515°C for the 2D model, calculated using an area integral, compared to 543°C for the 1D model (a significant over-prediction). Figure 3.13 reaffirms that predictions of insulation temperature are poor for both models.

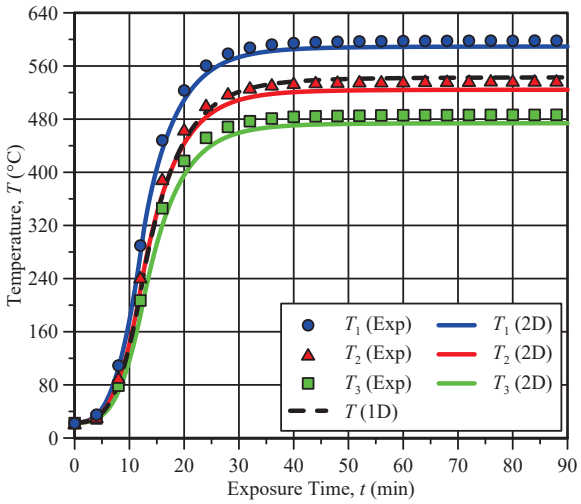

Figure 3.12: Steel plate temperatures for the Ramp50 exposure.

After 90 min, the temperatures measured are 441°C at T_4, 285°C at T_5, and 80°C at T_6. Again, temperatures are under-predicted significantly; in the worst case by 64°C (2D) and 69°C (1D) at T_5. Figure 3.14 shows the temperature gradient computed by the 2D model through the specimen assembly for the Ramp50 exposure at $t = 90$ min. The dashed lines in Fig. 3.14 indicate the boundaries between each material. There is a temperature variation of 115°C from centreline to edge at the bottom of the steel plate, a function of its high thermal conductivity, non-uniform surface boundary condition, and side heat losses. In contrast, the temperature of the insulation at its midpoint varies from 290°C at the centreline to 38°C at the edge. The cement board temperature does not rise significantly from ambient.

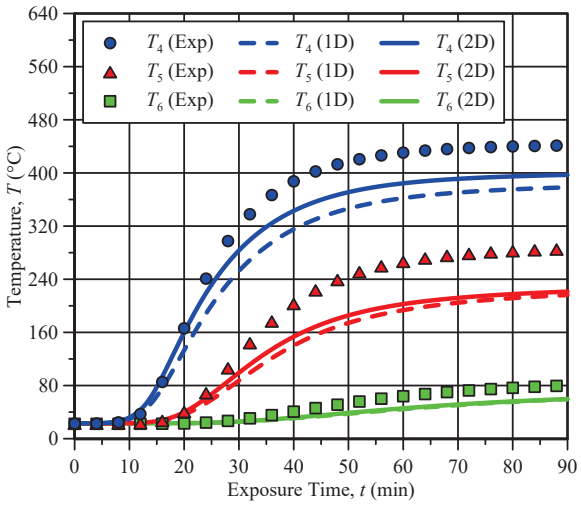

Figure 3.13: Insulation temperatures for the Ramp50 exposure.

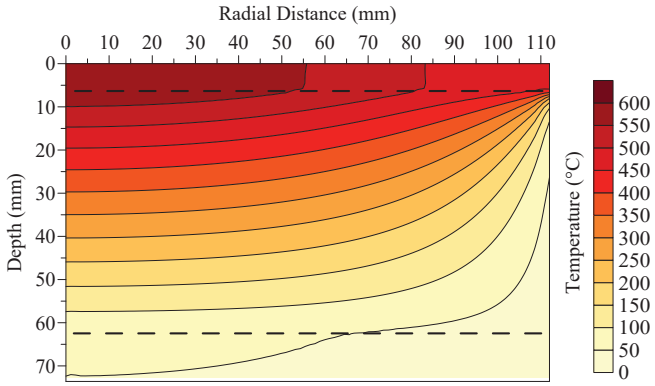

Figure 3.14: Temperature gradient of the specimen after 90 min of Ramp50 exposure as computed by the 2D axisymmetric model.

3.2.7 Discussion

The 2D model predicts temperatures on the bottom of the steel plate with good accuracy for both exposures, with slightly greater error at the higher irradiance. This section addresses the sensitivity of the model to input parameters.

A sensitivity analysis is conducted in order to assess the relative impact of the input parameters to the 2D model on the predicted results. The temperature on the bottom

of the steel plate at $r = 0$ and $t = 90$ min for the Ramp50 exposure is selected as the baseline parameter for comparison (589.3°C). Multipliers of 0.75 (-25%) and 1.25 (+25%) are applied to k, ρ, c_p, h_c, and ε. The parameters which have the most significant impact are k_A, $h_{c,top}$, and $\varepsilon_{A,top}$ (refer to Table 3.2). Density and specific heat capacity have more of an impact on model predictions during the initial stage of heating. The model is also run with the following changes in configuration:

- an adiabatic boundary condition imposed on the sides of the specimen assembly, resulting in an increase of 12.7°C;
- an adiabatic boundary condition imposed on the bottom of the cement board, resulting in an increase of 0.1°C;
- the cement board is neglected entirely, and an adiabatic boundary condition was imposed on the bottom of the fibre insulation, resulting in an increase of 1.8°C; and
- T_∞ is used in place of T_g in Eq. 3.3, resulting in a decrease of 20.7°C.

It is clear that the cement board has very little impact on the predicted temperature of the steel plate, and can be replaced entirely with an adiabatic boundary condition on the bottom of the insulation in future models. Furthermore, the assumption of an adiabatic side boundary condition is not justified, therefore accounting for the heat loss from the sides of the specimen assembly is necessary. The most significant changes occur when the ambient gas temperature,T_∞ is used in place of T_g for convection heat transfer on the top surface, and when a poor value of top surface emissivity is used. Therefore, the accuracy of this particular model is limited primarily by the specification of heat losses on the top surface. Accurate determination of surface emissivity and measurement of gas temperature near to the specimen surface is important for future experiments.

The results confirm that the average temperature predicted by the 1D model are significantly lower than those measured experimentally at the centreline, while the 2D model is able to predict centreline and edge temperatures with good accuracy. Furthermore, the average temperature computed by the 1D model is significantly greater than that predicted by the 2D model, which can presumably be attributed to side heat losses being neglected in the 1D model. These findings make it clear that a 1D model formulation is not appropriate for predictions of heat transfer in this experiment involving a large cylindrical specimen.

Although the 2D axisymmetric heat transfer model is able to accurately predict the measured steel temperatures, it must be noted that there is some uncertainty in the thermophysical properties used for the steel. In this study, steel properties are taken from

Table 3.2: Sensitivity of the 2D axisymmetric model to input parameters (values are the change from the baseline temperature of 589.3°C at the bottom-centre of the steel plate for the Ramp50 exposure after 90 min).

Parameter	-25% Change (°C)	+25% Change (°C)
k_A	+13.3	-10.1
k_B	+2.2	-2.1
k_C	0.0	0.0
ρ_A	0.0	0.0
ρ_B	+0.1	-0.1
ρ_C	0.0	0.0
$c_{p,A}$	0.0	0.0
$c_{p,B}$	+0.1	-0.1
$c_{p,C}$	0.0	0.0
$h_{c,top}$	+5.3	-5.1
$h_{c,sides}$	+0.4	-0.4
$h_{c,bottom}$	0.0	0.0
$\varepsilon_{A,top}$	-23.9	+1.5[a]
$\varepsilon_{A,sides}$	+1.7	-0.1[a]
ε_B	+0.3	-0.2[a]
ε_C	0.0	0.0

[a] Emissivity is increased to a maximum value of 1.

Zhang and Delichatsios [89] based on the similarity of experiment. Notably, the thermal conductivity used here is constant, despite the known temperature-dependence of the property. When this experimental methodology is applied to other materials, which may undergo thermal decomposition, it will be important to obtain independent measurements of the temperature-dependent thermophysical properties to ensure model accuracy.

It is apparent from the results that neither model was able to predict the temperature gradient through the depth of the insulation with accuracy. This can undoubtedly be attributed to a poor selection of thermophysical properties for the insulation, notably the thermal conductivity. The function given in Table 3.1 is derived from manufacturer data for the insulation in an uncompressed state; it is likely that the thermal conductivity of

the insulation used here, compressed by 25%, will be different. Since compression removes air from the fibre matrix, it is reasonable to presume that the thermal conductivity will be greater in a compressed state, resulting in higher predicted temperatures, which would be in agreement with the results presented above. An inverse model could be used with the results presented here to compute the effective thermal conductivity of the compressed insulation.

It has been demonstrated that the modified cone calorimeter experiment presented in this work is able to facilitate a non-uniform transient exposure with well characterized thermal boundary conditions. Furthermore, it has been shown that a 2D-axisymmetric model is able to accurately predict a non-uniform thermal gradient through a non-degrading specimen.

3.3 Computational Fluid Dynamics Simulations

As an intermediate step to complete fire simulations, 3D computational fluid dynamics simulations (CFD) are undertaken to reproduce the thermal effects of the cone calorimeter test on a specimen. Single material specimens may be readily implemented. In the present study, the modified cone calorimeter experiment proposed in Section 3.1 is simulated using the multi-layer specimen of steel, insulation, and cement board.

3.3.1 Modelling Approach

A notable difference in the development of these CFD simulations is the difference in prescribed formulation. Within OpenFOAM, the implementation of heat transfer effects is already incorporated by the developers of the code, and only need to be selected appropriately. Whereas, in the finite difference model, every correlation is manually prescribed. For these simulations the heat transfer effects on the temperature of the specimen is of primary interest and resolved by conservation of energy, shown in Eq. 3.16. Conduction, convection, and radiation are included in Eq. 3.16.

$$\frac{\partial \overline{\rho}\widetilde{h}}{\partial t} + \frac{\partial \overline{\rho}\widetilde{u_j}\widetilde{h}}{\partial x_j} = \frac{\partial}{\partial x_j}(\overline{\rho}(D_h + \frac{v_t}{Pr_t})\frac{\partial \widetilde{h}}{\partial x_j}) - \Delta \cdot \dot{q_r}''' + \dot{q}''', \tag{3.16}$$

where D_h is the thermal laminar diffusion coefficient, Pr_t the turbulent Prandtl number, h the enthalpy, $\dot{q_r}'''$ the radiative heat flux, and $\dot{q}'''$ the HRR due to chemical reactions.

Conduction is calculated within the specimen. No contact resistance is applied between the layers. When dealing with the fluid domain, a simplification applied in the present study is that of "frozen flow." Since the air flow around the specimen is anticipated to have a small impact on the heat transfer, the flow field is assumed to be stationary. This assumption neglects the effects of convective heat transfer. The pressure and velocity fields are assumed to be constant. The computational time is significantly reduced and the numerical stability of the solution enhanced. Due to this "frozen flow" assumption, many of the terms present in Eq. 3.16 are negligible, due to $u = 0$. An important remaining term is $\dot{q_r}'''$, the radiative heat flux.

There are several modelling options for the treatment of radiation. A finite volume discrete ordinates method (fvDOM) is selected for this case. This technique solves the RTE over a number of different directions taking into account the properties of the participating medium. Rays at discrete angles are emitted from each surface and the intensity of each is calculated, taking into account the properties of the medium it passes through. These properties include absorptivity, transitivity, and emissivity. As air is the medium, which has low scattering and absorbing properties, a constant absorption-emission model is selected. A gray assumption is assumed for the surfaces, where absorptivity is equivalent to emissivity.

3.3.2 Numerical Implementation

The domain is represented by four solid regions surrounded by a fluid region. The solid regions consist of the cone heater and the three layers of the specimen: steel, insulation, and cement board. Due to the complex nature of the cone dimensions and the difficulty of modelling the geometry, the cone is simplified to a solid ring. The equivalent projected surface area is used as the dimensions. A view of the solid regions of the domain is shown in Fig. 3.15. As seen, the specimen (r=112 mm) is wider than the heater diameter (r=80 mm). A 25 mm air gap separates the cone from the specimen. The steel is 6.2 mm thick, insulation 56.0 mm thick, and cement board 10.6 mm thick. Not pictured is the surrounding domain of ambient air encompassing a 1 m^2 area. The domain is divided into finite cells. The mesh is fairly uniform, with cell size increasing towards the outer radius due to the increasing circumference of the specimen. Figure 3.16 displays the final discretization mesh selected. The average cell size in the radial direction is 4.4 mm. Into the depth of the specimen, the steel cell size is 1.24 mm thick, insulation 1.56 mm thick, and cement board 3.53 mm thick.

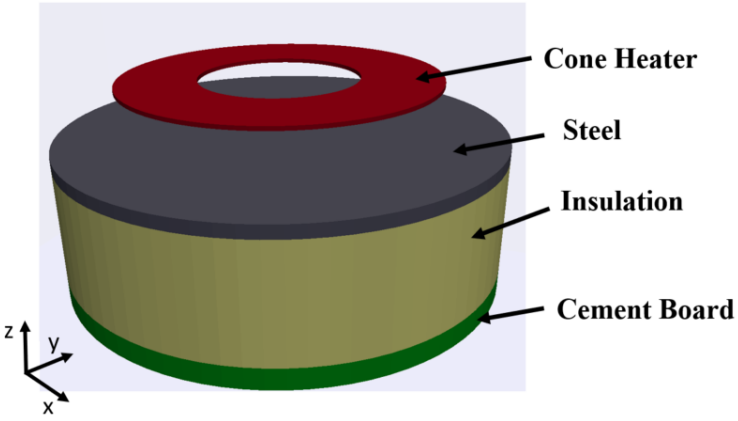

Figure 3.15: Representation of heater and multi-layer specimen in computational domain.

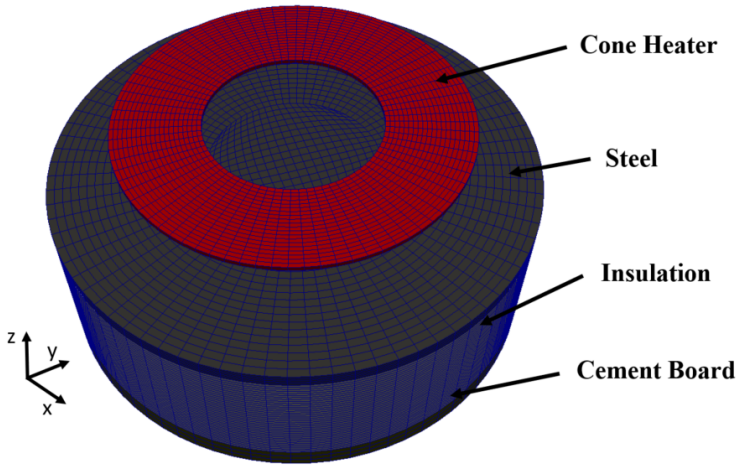

Figure 3.16: Final mesh (air domain excluded for clarity).

Prescribed Conditions Fewer conditions are prescribed in these CFD simulations compared to the finite difference calculations in Section 3.2. The requirements are: boundary conditions initial conditions, and material properties.

Two types of boundary conditions are applied, one on the extent of the computational domain, and one between the solid and fluid interface. All domain boundaries are prescribed at ambient temperatures (T=20°C), and pressures (P=101325 Pa). The experimentally recorded temperature for the cone heater is prescribed as an input to the

simulations. As the cone heater temperature (T_c) is not experimentally measured, it is calculated from the experimental heat flux ($q"_{exp}$). Assuming the cone heater can be treated as a black body, T_c is determined from Eq. 3.17.

$$T_c = (\frac{q''_{exp}}{F_{c-s}} + T_\infty^4)^{1/4}, \tag{3.17}$$

where F_{c-s} is the view factor from the cone to the centreline. The resultant transient T_c values are applied uniformly to the simulated cone region and updated every second, for a total of 5400 s of exposure. For the Ramp25 case, the steady state T_c is 598.8°C and for Ramp50 T_c is 762.4°C. The boundaries of the solid specimen, exposed to the fluid, are calculated using a radiative boundary condition. This boundary calculates a net heat flux at each boundary cell to determine the direction of energy transfer.

All initial conditions are set to ambient conditions, specified above. Second order discretization schemes are used in time and space. The temperature dependent thermophysical properties (k, ρ and c_p) for each of the three materials is implemented, as shown in Table 3.1.

3.3.3 Mesh Independence

Before the final results are generated, a mesh dependence study is performed to ensure the temperature predictions are independent of the mesh resolution. Several meshes are created and the same case run on each. A comparison is made to determine minimum amount of cells which is sufficient for further refinements to have negligible impact on the results. It is ideal to not use too large of mesh for large computational times. In this study, three meshes are considered, a coarse mesh with 89 000 cells, a medium mesh with 270 000 cells, and a fine mesh with 500 000 cells. Three temperature locations are shown in Fig. 3.17. T_1, T_3, and T_5 are compared with minimal differences found at the steel locations (T_1 and T_3). A small difference is found at T_2 (1.1%) between the 90 000 and 270 000 cell mesh. This difference reduced to 0.5% between the 270 000 and 500 000 cell mesh, therefore, the 270 000 cell mesh.

3.3.4 Results

The modelled temperatures at three locations on the steel plate and three locations in the insulation layer are compared to the experimental values. T_1, T_2, T_3 are on the unexposed side of the steel plate and increase in radial location outward. T_4, T_5, T_6 are on the

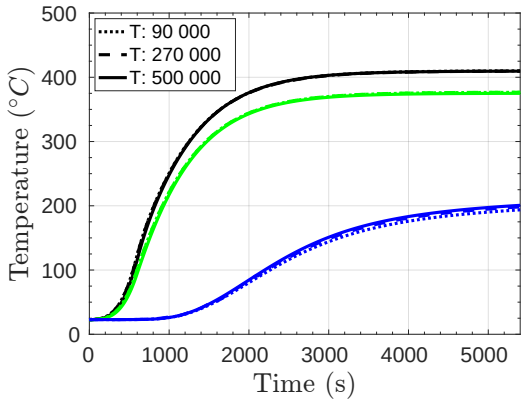

Figure 3.17: Grid independence study at T_1, T_3, and T_5 for three levels of mesh refinement.

centerline and increasing in depth through the insulation layer. A discussion of the results and possible reasons for any discrepancies is made.

Ramp25

Starting with the lower irradiance test, as seen in Fig. 3.18, the predicted temperature on the underside of the steel plate is compared with the experimental values. The temperatures rise to a maximum of 415°C at steady state in 2000 s in the experiment but take closer to 3000 s in the simulation. These steady state temperatures agree well, however the transient profile is off by a maximum of 48.6°C, where the simulated temperatures lags behind the experiments during heating. At steady state, the CFD simulation under-predicts the experiment by 6.1°C at the centreline (T_1), over-predicts by 9.4°C at T_2 (r=70 mm), and over-predicts by 17.2°C at T_3 (r=100 mm). A more uniform temperature is predicted across the surface, suggesting that not enough irradiance is received at the centreline and too much irradiance is received at the edges. This is likely caused by the simplification of the cone heater geometry as a disc. In Fig. 3.19 the temperature predictions through the insulation layer are shown. The experimental temperature at T_4 starts to increase after 750 s. Steady state is eventually reached after an additional 3000 s at a temperature of 298°C. T_5 and T_6 take longer before starting to increase and reach lower steady state temperatures, at 185°C and 71°C, respectively. In this case there is a slight over-prediction of the predicted temperatures at steady state, 18.9°C at T_4, 24.4°C at T_5 and 23.2°C at T_6. The bottom location (T_6) predicted temperatures do not quite reach steady state as

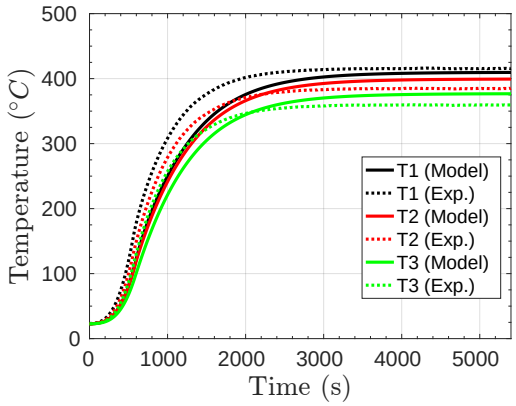

Figure 3.18: Ramp25 temperatures at underside of steel plate.

observed in the experiments. These discrepancies are likely due to inaccurate material properties in the simulations, since the agreement for the steel is good.

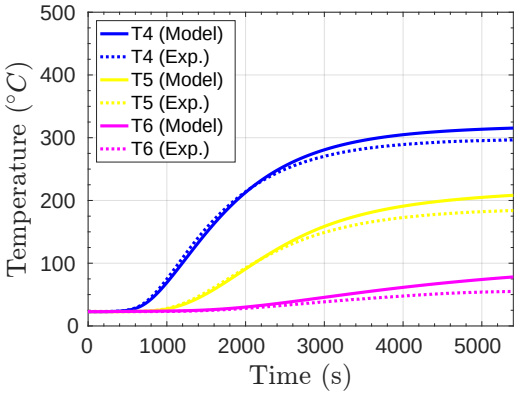

Figure 3.19: Ramp25 temperatures through insulation layer.

Ramp50

For the higher irradiance test, the temperatures are shown in Fig. 3.20. A similar

transient profile is observed as in the Ramp50 test, however the maximum temperatures reached at steady state are significantly higher (596°C vs. 416°C in the experiment). In this case the centreline temperature (T_1) is under-predicted by 49.6°C, at r=70 mm, T_2 is under-predicted by 6.7°C and at the outer edge, T_3 is over-predicted by 4.7°C. The magnitudes of these discrepancies are now higher compared to the Ramp25 case, which is expected due to the larger magnitude of heat flux. This reinforces the idea that the representation of the cone heater is oversimplified, the surface not receiving enough heat to the centreline due to the flat representation of the cone.

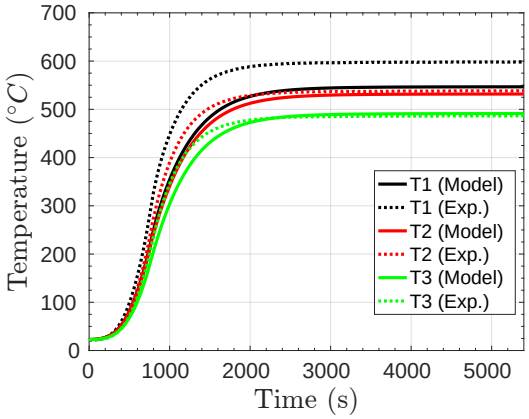

Figure 3.20: Ramp50 temperatures at underside of steel plate.

The insulation temperatures are presented in Fig. 3.21. The top two locations reach nearly steady state by the end of the test, the predictions are quite good here, with an under-prediction of 6.4°C. At a depth of 2/3 into the insulation layer (R_5) the simulation under-predicts by 14°C. The bottom location, the simulation over-predicts by 33.8°C and does not quite reach steady state.

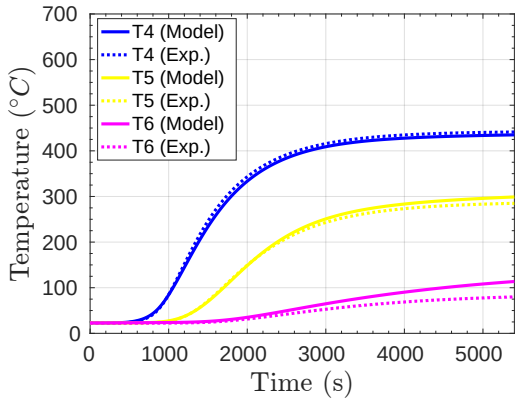

Figure 3.21: Ramp50 temperatures at underside of steel plate.

3.4 Conclusions

Due to the difficulty in characterizing and modelling the standard cone calorimeter experiment, a modified experimental setup is implemented which adopts a large, cylindrical specimen aligned co-axially with the cone heater. In the present study, a non-degrading material (A36 steel) is selected in the experiments and a transient exposure applied. Both 1D and 2D axisymmetric finite difference heat transfer formulations are developed and solved numerically to predict the temperature at a total of six locations varying in depth and radial distance. Modelled results compare favourably with experimental measurements. It is demonstrated that, for the modified experimental configuration in the current work, a 2D axisymmetric model yields results with improved accuracy over a 1D model. Additionally, the effects of specimen degradation using a simple pyrolysis model are available in the simulations and the "apparent heat capacity" method implemented, to account for the bulk material properties.

CFD simulations are developed for the same experimental conditions and fewer assumptions are applied. The most important difference is prescribing the cone temperature and representing the geometry in the computational domain, in contrast to explicitly defining the well characterized boundary conditions on the surfaces of the specimens. Similar agreement to the experimental results are obtained to the finite difference model. The steel temperatures for the Ramp50 test are not as well predicted due to the simplified

representation of the cone as a flat disc. As seen with the finite difference model, the insulation temperature predictions had some discrepancy due to the uncertainties in the material properties. It is found these CFD simulations adequately account for conjugate heat transfer treatment of the cone calorimeter experiment.

Chapter 4

Single Compartment Fire

Based upon the progress made with the small-scale CFD simulations, a full-scale compartment fire is investigated. The heat transfer modelling and the CFD approach taken in Section 3.3 still apply, however now the flow field is necessary to be accounted for. The compartment fire experiment is introduced, the additional modelling steps taken, the numerical implementation, and finally the comparison of the simulations to the experimental results.

4.1 Experimental Details

The test facility is a compartment of size 4 m x 4 m x 4 m with a 0.2 m x 2 m door in the centre of one wall, as seen in Fig. 4.1. The pool fire is CH_3OH with a diameter of 60 cm and placed in the center of the room. The MLR is measured for the duration of the burn and a constant fuel height feed system is used to maintain a liquid fuel level of 3 cm below the rim (12 cm above the ground). The door remains open for the duration of the test. The room is built with clay bricks with a thickness of 23 cm and a cement-sand plaster on each side of the bricks, with a thickness of 2 cm. The floor and ceiling are made of concrete with the ceiling being 14 cm thick [65]. Thermocouple rakes are the primary instrumentation used. An array of 16 K type thermocouples are mounted 1 m below the ceiling in an uniform 4 x 4 grid. Referring to Fig. 4.1, thermocouple rake B is directly over the centre of the pool to measure flame temperature. Rake D is centered in the doorway to determine temperatures and to find the approximate level of the neutral plane. Rake C is placed in a corner and extended from the ground to the ceiling to capture the stratification in the room and hot layer height [64].

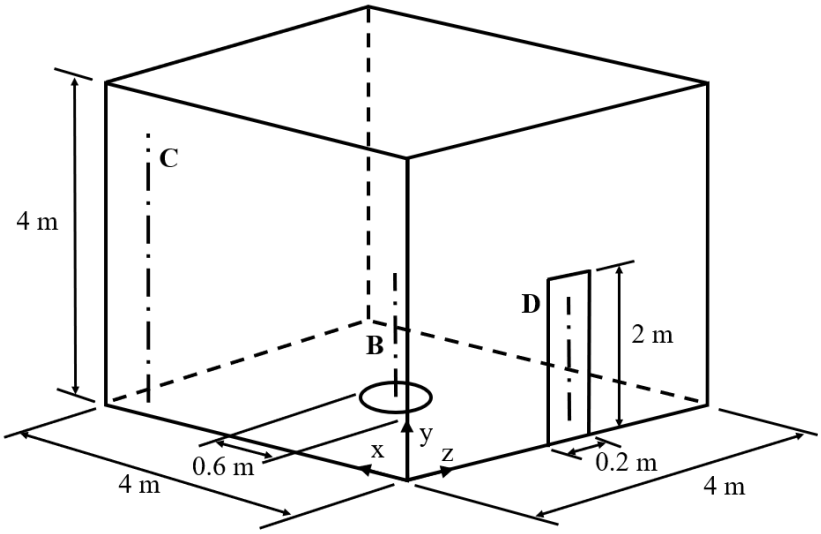

Figure 4.1: Schematic of the room setup and instrumentation; reproduced from [64].

4.2 Modelling Approach

The governing equations needed for the fluid domain are introduced, which are slightly different than those presented in Section 3.3. The turbulence approach, chemistry selected and modifications to the heat transfer models are outlined.

4.2.1 Transport Equations

FireFOAM solves a modified set of governing equations for mass, momentum, energy, and species transport. These equations are filtered and Favre-averaged, also known as mass-weighted averaged, which is typically done in flows where large variations in density occur such as flows with combustion [22]. Conservation of mass is shown in Eq. 4.1, conservation of momentum in Eq. 4.2, energy transport in Eq. 4.3, and species transport in Eq. 4.4, where $(\tilde{\cdot})$ represents the Favre-averaged quantity [1].

$$\frac{\partial \overline{\rho}}{\partial t} + \frac{\partial \overline{\rho} \widetilde{u_j}}{\partial x_j} = 0, \tag{4.1}$$

where ρ is the density, t the time, u the velocity, and x_j the Cartesian coordinate.

$$\frac{\partial \overline{\rho}\widetilde{u_i}}{\partial t} + \frac{\partial \overline{\rho}\widetilde{u_i}\widetilde{u_j}}{\partial x_j} = \frac{\partial \overline{\rho}}{\partial x_j} + \frac{\partial}{\partial x_j}(\overline{\rho}(v + v_t)(\frac{\partial \widetilde{u_i}}{\partial x_j} + \frac{\partial \widetilde{u_j}}{\partial x_i} - \frac{2\partial \widetilde{u_k}}{3\partial x_k}\delta_{ij})) + \overline{\rho}g_i, \tag{4.2}$$

where p is the pressure, g the gravitational force, v the kinematic viscosity, v_t the turbulent kinematic viscosity, and δ_{ij} the Kronecker delta.

$$\frac{\partial \overline{\rho}\widetilde{h}}{\partial t} + \frac{\partial \overline{\rho}\widetilde{u_j}\widetilde{h}}{\partial x_j} = \frac{D\overline{\rho}}{Dt} + \frac{\partial}{\partial x_j}(\overline{\rho}(D_h + \frac{v_t}{Pr_t})\frac{\partial \widetilde{h}}{\partial x_j}) - \nabla \cdot \dot{q_r}''' + \dot{q}''', \tag{4.3}$$

where D_h is the thermal laminar diffusion coefficient, Pr_t the turbulent Prandlt ($Pr_t = 1$ by default), h the enthalpy, $\dot{q_r}'''$ the radiative heat flux, and $\dot{q}'''$ the HRR due to chemical reactions.

$$\frac{\partial \overline{\rho}\widetilde{Y_k}}{\partial t} + \frac{\partial \overline{\rho}\widetilde{u_j}\widetilde{Y_k}}{\partial x_j} = \frac{\partial}{\partial x_j}(\overline{\rho}(D_Y + \frac{v_t}{Sc_t})\frac{\partial \widetilde{Y_k}}{\partial x_j}) + \overline{\dot{w}}_{Y_k}, \tag{4.4}$$

where Y is the species mass fraction, Sc_t the turbulent Schmidt number, and $\dot{w}$ the chemical reaction rate.

4.2.2 Turbulence

In the present study, LES is selected. The conservation of momentum equation, specific to the LES implementation, is presented in Eq. 4.5 [1].

$$\frac{\partial \overline{\rho}\tilde{u_i}}{\partial t} + \frac{\partial \overline{\rho}\tilde{u_i}\tilde{u_j}}{\partial x_j} = -\frac{\partial \overline{\rho}}{\partial x_i} + \frac{\partial \overline{\sigma}_{ij}}{\partial x_j} - \frac{\partial \tau_{ij}^{sgs}}{\partial x_j}, \tag{4.5}$$

where σ_{ij} is the viscous stress tensor, τ_{ij}^{sgs} the SGS viscous stress tensor, and p the pressure.

$$\overline{\sigma}_{ij} = \mu(2\tilde{S_{ij}} - \frac{2}{3}\tilde{S_{kk}}\delta_{ij}), \tag{4.6}$$

where μ is the dynamic viscosity, S the rate of strain tensor, and δ the Kronecker delta.

$$\tilde{S_{ij}} = \frac{1}{2}(\frac{\partial \tilde{u_i}}{\partial x_j} + \frac{\partial \tilde{u_j}}{\partial x_i}), \tag{4.7}$$

$$\tau_{ij}^{sgs} = \overline{\rho}(\widetilde{u_i u_j} - \tilde{u_i}\tilde{u_j}). \tag{4.8}$$

The smaller scales are modelled using a SGS model to resolve τ_{ij}^{sgs}. To differentiate the turbulent length scales, an implicit filter is applied, as seen in Fig. 4.2. Anything below

this filter size is modelled, whereas anything above is solved directly for. The goal is to use a filter range in the inertial sub-range so that the majority of the kinetic turbulent energy is resolved and a smaller amount modelled using the specific SGS model. A classification of SGS models is those that use the eddy-viscosity approach. A turbulent viscosity term (ν_t) accounts for the effects of turbulence and includes empirical coefficients. These coefficients can either be static or dynamic (recalculated at each iteration). Dissipation of kinetic energy at sub-grid scales is treated in an analogous way to molecular diffusion. The SGS

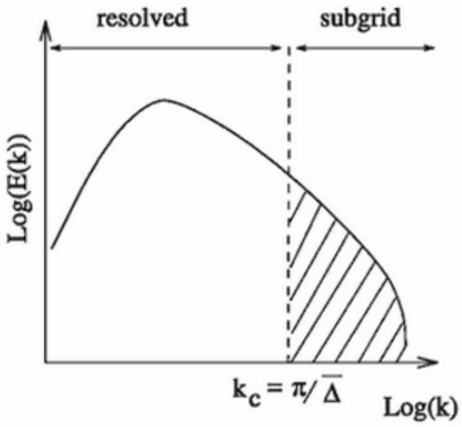

Figure 4.2: Resolved and modelled energy vs. wave number. Reproduced from [63].

turbulent kinetic energy, k_{sgs}, is defined in Eq. 4.9, as half of the trace of the Reynolds stress tensor. The present study employs a k-equation eddy viscosity model. An extra transport equation for k_{sgs} is applied for turbulence closure, as shown in Eq. 4.10, where the right-hand side (RHS) includes the effects of production, dissipation, and diffusion, respectively.

$$k_{sgs} = \frac{1}{2}(\overline{u_i^2} - \overline{u_i}^2), \tag{4.9}$$

$$\frac{\partial \overline{\rho} k_{sgs}}{\partial t} + \frac{\partial \overline{\rho} k_{sgs} \tilde{u_j}}{\partial x_i} = \overline{\rho}(\tau_{ij}\frac{\partial \tilde{u_i}}{\partial x_j}) - \overline{\rho} C_\epsilon \frac{k_{sgs}^{3/2}}{\Delta} + \frac{\partial}{\partial x_i}(\frac{\overline{\rho}(\nu + \nu_t)}{Pr_t}\frac{\partial k_{sgs}}{\partial x_i}), \tag{4.10}$$

where τ_{ij} is the SGS stresses, C_ϵ and σ_k are model constants, and Δ the filter size $\Delta = (\Delta x \Delta y \Delta z)^{1/3}$ calculated based on the local grid size. In this modelling approach, the SGS stress term τ_{ij}^{sgs} is also given by Eq. 4.11.

$$\tau_{ij}^{sgs} = \frac{2}{3}k_{sgs} - 2\nu_t \overline{S_{ij}}\delta_{ij}, \tag{4.11}$$

where δ is the Kronecker delta. Finally, the eddy viscosity term is expressed as

$$\nu_t = C_k \sqrt{k_{sgs}} \Delta. \tag{4.12}$$

Default static coefficients of $C_k = 0.05$, $C_\epsilon = 1.048$, and $\sigma_k = 1.0$ are selected [87].

4.2.3 Chemistry

Unlike with laminar combustion, the turbulence effects are critical for accurate modelling in turbulent combustion. In the present study, combustion is modelled with the eddy dissipation concept (EDC) approach. This approach only works for irreversible global reactions. Infinitely fast chemistry is assumed, where if fuel and oxidizer are mixed then the mixture is 'burnt' or the reaction has occurred. This assumes that the Damköhler number ($Da = \frac{\tau_T}{\tau_c}$) $>> 1$, where the chemical time scale, τ_c, is assumed to be much smaller than the flow time scale τ_T [23]. The reaction rate, $\overline{\dot{w}}_{Y_k}$, seen in Eq. 4.13, is governed by a time scale determined from the minimum of the turbulence and diffusion time scales [1]. The specific turbulence model dictates the turbulence mixing time scale. In Eq. 4.13, Y_F and Y_{O_2} represent fuel and O_2 mass fractions, r_s the stoichiometric O_2-to-fuel ratio, and C_{EDC} and C_d are model coefficients.

$$\overline{\dot{w}}_{Y_k} = \frac{\rho}{min(\tau_t / C_{EDC}, \tau_{diff} / C_d)} min(Y_F, Y_{O_2} / r_s) \tag{4.13}$$

For chemistry, a one-step reaction is used as shown in Eq. 4.14. This is a simplification, as in reality many intermediate steps take place and include products including NO_x, CO, OH, and hydrogen (H), which is converted to H_2O at a rapid rate. Nitrogen (N_2) is present but inert in the reaction. Complete combustion is assumed. Since CH_3OH produces a clean burning flame at atmospheric pressure, soot may be neglected in the present case.

$$CH_3OH + 1.5O_2 + 5.76N_2 \rightarrow CO_2 + 2H_2O + 5.76N_2 \tag{4.14}$$

4.2.4 Heat Transfer Models

The radiation model implemented is finite volume Discrete Ordinances Method (fvDOM). This technique solves the RTE over a number of different directions, taking into account the properties of the participating medium. To simplify the computation of the RTE, an experimentally determined constant (χ_r) is used to represent the amount of heat from combustion lost to radiation. For CH_3OH pool fires, a value of 0.15 for χ_r is found to be

appropriate [28]. The participating effects include absorptivity and emissivity of the gases within the compartment. Therefore, the main products of combustion: CO_2 and H_2O, need to be accounted for. A mean gray absorption model is used which spectrally averages properties for the gas coefficients. Planck mean absorption coefficients ($a_{p,i}$) of each species are combined into an overall absorption constant (κ_g), as shown in Eq. 4.15. The Planck coefficients are tabulated according to fourth order polynomials determined by Wakatsuki [82].

$$\kappa_g = \sum_i a_{p,i}\ p_i, \tag{4.15}$$

where p is partial pressure of species i. An additional effect of radiation through a medium is scattering, which is taken into account using a constant scattering approach. Constant scattering coefficients of 0.01 are used for all species. For the radiation model, the amount of rays is set to 48, as determined by Chatterjee et al. [21] to be sufficient for characterizing the radiative exchange within the fire.

The walls are modelled to account for heat loss out of the compartment through the walls. Radiative and convective heat transfer to the walls are taken into account, as well as conduction through the wall, and radiation and convection to the ambient on the non-fire side of the wall. This is accomplished through a simplified 1D heat transfer approach to reduce computational time where the emissivity, conductivity, density, and specific heat of the wall materials are considered. Thermophysical properties, in particular specific heat, of all species are based upon NASA polynomials within specified temperature ranges and are tabulated from the coefficients recorded by McBride et al. [50].

Finally, a thermocouple (TC) model is included based on Eq. 4.16, to account for the heat transfer and thermal inertia of thermocouple beads [1]. The thermocouple bead is modelled as a sphere, where ρ is the density, C_p the specific heat, V the volume, T the temperature, ϵ the emissivity, and A the surface area. G is the average irradiance received, h the convective heat transfer coefficient, T_g the gas temperature, and σ the Stefan-Boltzmann constant.

$$\rho_{TC} C_{p,TC} V_{TC} \frac{dT_{TC}}{dt} = \epsilon_{TC}(G - \sigma T_{TC}^4) A_{TC} + h(T_g - T_{TC}) A_{TC}. \tag{4.16}$$

4.3 Numerical Implementation

The computational domain is defined according to the geometry of the room, discretized, thermophysical properties tabulated, model settings selected, and boundary conditions

applied. The interior dimensions of the room are modelled, as well as the walls with the appropriate dimensions. An 'air box' is added to the computational domain outside the door, as seen in Fig. 4.3. The fuel inlet can be seen inside the compartment with the 'air box' on the exterior of the thin door. The 'air box' is added to move the effect of the boundary conditions further away from the fire source. This is an approach to improve the stability of the solution and reduce the velocity fluctuations present at the domain boundaries [20, 38, 49, 66]. The boundaries at the extent of the air box are set to be

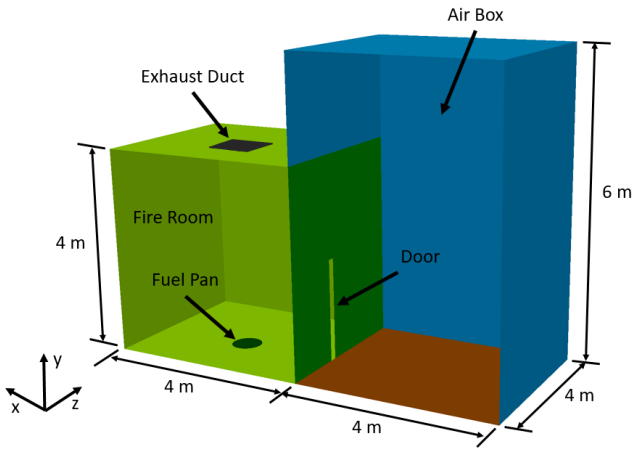

Figure 4.3: Schematic of computational domain.

pressure driven velocity conditions, where they can act as an inlet or outlet at any point depending upon the calculated pressure. The walls, ceiling, and ground are set to a no-slip condition for velocity with zero gradient for most other properties. The unexposed parts of the walls are treated free to convect and radiate to the surroundings, and any air flow into the domain was set to ambient temperature. The 60 cm diameter pool fire is modelled as a mass flow rate inlet condition, where the flow is CH_3OH vapour at the boiling point temperature [20]. An experimentally determined MLR the input condition, which has a steady state value of approximately 4.6 g/s.

The PIMPLE algorithm is selected which is a transient algorithm and a combination of the semi-implicit method for pressure-linked equations (SIMPLE) and pressure-implicit split-operator (PISO) algorithms. This algorithm works on the premise of enforcing mass conservation, via a pressure equation, then a correction to velocity to ensure momentum conservation. A negligible difference between the first and second order temporal schemes is found. Thus, first order temporal discretization is selected to reduce computation time.

Spatial schemes are second order accurate. A maximum Courant number of 0.8 is enforced and the time step initially set to 0.001 s and allowed to vary according to the Courant number limit.

The final mesh selected has a relatively uniform density of cells, with refinement in the flame region and coarser the farther away from the flame, as seen in Fig. 4.4. The mesh has a total of 750 000 cells with an average side length of 5 cm within the compartment, and an average side length of 2.5 cm in the flame region.

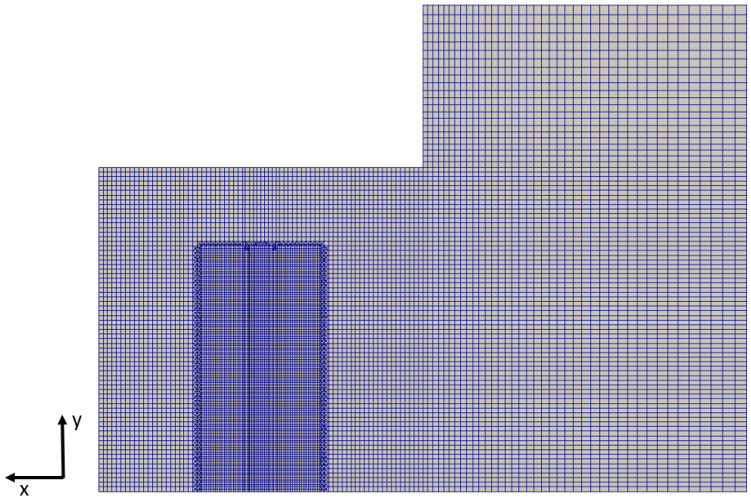

Figure 4.4: Cross-sectional view of computational mesh.

4.4 Results

The steady state experimental MLR is 0.0044 kg/s, after the initial growth period. This corresponds to an area weighted MLR of 0.0155 kg/(s m^2), which agrees well to the theoretical infinite diameter MLR of 0.017 kg/(s m^2) for CH_3OH pools [28]. The slightly lower experimental value is due to the effects of the lip of the burner, which inhibit the burning rate.

The temperature profile is shown in Fig. 4.5. The fire compartment has filled with hot gases that escape through the doorway. The neutral plane is found to be approximately halfway up the height, at 0.9 m in the simulation, which matches the height reported in

the experiment. Below this height, cold ambient air flows into the compartment to fuel the fire and above this height hot gases flow exit the compartment. The flame is seen to be blown over towards the rear of the compartment due to the incoming air. The flame is then centered over the edge of the pool rather than the center.

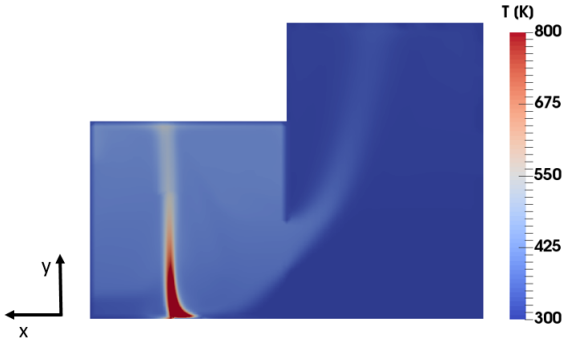

Figure 4.5: Cross-sectional view of steady state temperature contour.

Flame temperatures are compared with experimental data and shown in Fig. 4.6, at 3 min and 30 min after ignition. At 3 min, the model predicts the temperatures well with an average under-prediction of 64° from 0.5-1 m in height. At 30 min, the model significantly under-predicts the temperatures. This under-prediction is due to the flame being blown to the side due to the velocity of air through the door. Therefore, the temperatures shown are not the true flame temperatures. A clear separation of hot layer and incoming air is inferred from Fig. 4.7, at a height of 0.9 m, which matches what is experimentally observed. At 30 min, anything above 0.9 m is at elevated temperatures indicative of the hot gas layer leaving the room. The simulation under-predicts the temperature by approximately 20 K. A large under-prediction is found after 3 min as the hot gas layer has only just begin to form in the LES results.

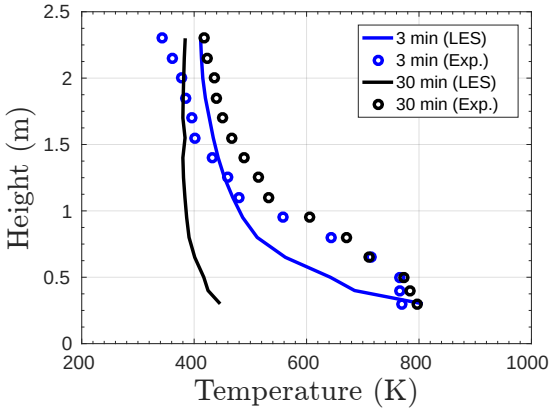

Figure 4.6: Steady state temperatures above pool centerline.

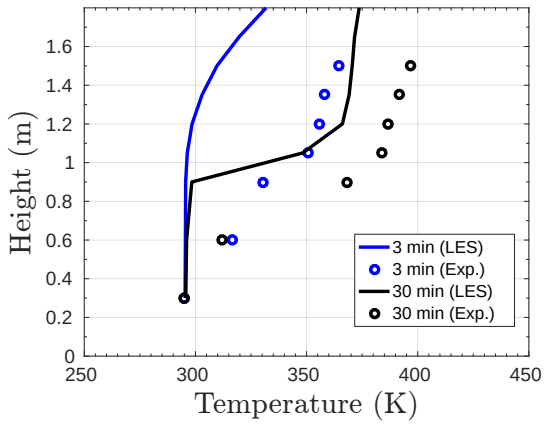

Figure 4.7: Steady state temperatures at doorway.

Referring to the corner thermocouple rake, shown in Fig. 4.8, the experiment resulted in a uniform hot layer temperature at both the 3 minute and 30 minute mark, where the temperature is approximately constant above 1 m from the ground. At 3 min, the average hot layer temperature is 380 K, which increases to 415 K at 30 min. The simulation

predicts a more gradual increase in temperature with respect to height, generally under-predicting the temperatures in the lower 3 m of the room and reaching approximately the same temperature at ceiling level. The numerical predictions at 30 min are closer to the experiment, showing a uniform hot layer temperature for the upper 1.5 m with an average under-prediction of 13 K at this near-ceiling height.

Experimental and predicted transient temperature profiles for the upper layer are displayed in Fig. 4.9. Good agreement is found between the model and experimental results at this near ceiling height. The simulation over-predicts the temperature during the growth period and under-predicts by an average of 9 K during the near steady state period of the burn.

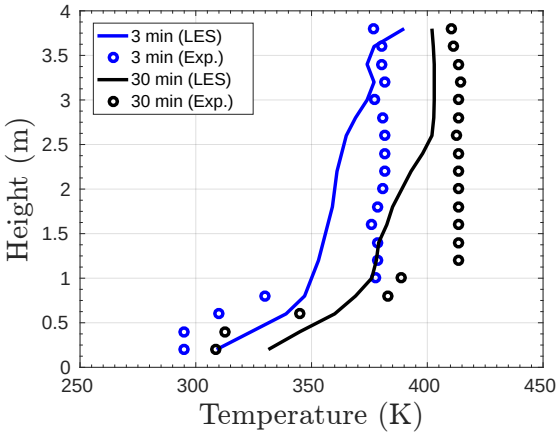

Figure 4.8: Steady state temperatures in back corner.

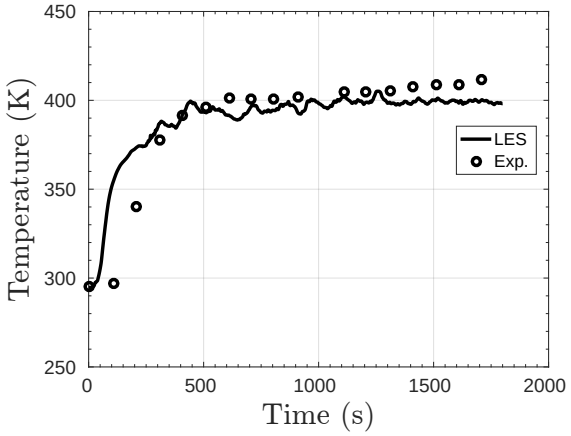

Figure 4.9: Transient temperatures in upper layer.

4.5 Conclusions

A fire simulation is completed and compared to a compartment pool fire experiment. Thermocouples are the primary instrumentation present, and a constant height of fuel in the fuel pan is maintained over the 30 minute fire. The simulations evolved to include the walls and a simulated 'air box' where the domain outside the door is extended to reduce the effect of the boundaries and better capture the flow behaviour within the room. Overall, temperatures in the upper part of the compartment are well predicted, however the constant hot layer temperature zone is not as large in the simulation. In the flame region and lower half of the room the temperatures are poorly predicted. In general, better numerical agreement is found at the 30 minute mark compared to the 3 minute mark for most locations. The exception is the flame region where the simulated flame is blown over due to the incoming ambient air through the doorway. The neutral plane height is predicted well with a clear transition 0.9 m above the ground, which is the same height observed in the experiment.

Chapter 5

Different Ventilated Compartment Fire Modelling

In addition to the challenges of accurate fire modelling, including radiation, combustion, and turbulence treatment, under-ventilated conditions pose further complications and difficulties. Increased chemistry and combustion model complexity are needed to account for the products of incomplete combustion and possible flame extinction. The numerical simulations presented in this Chapter contain many similarities with the modelling approach in Chapter 4, including the same turbulence and radiation modelling. The main modification is in the combustion modelling and associated addition of a chemistry solver. These modelling changes are outlined, then the presented numerical results are compared with these experimental results and compared with previously published numerical results [38]. The flow environment and differences between the cases are highlighted before conclusions drawn to summarize the attributes of the model.

5.1 Experimental Details

A set of experimental tests is selected in which a C_7H_{16} pool is burned in a ISO 9705 standard room with a single door opening. These tests are performed by Hwang et al. [38] and consist of; an under-ventilated fire with a restricted door opening and an over-ventilated fire case with a nominal sized door opening. Temperatures and product species concentrations are measured in multiple locations.

The test facility is a compartment built to ISO 9705 standards with an internal size of 3.6 m long $\times$ 2.4 m wide $\times$ 2.4 m high with a 2 m high door in the centre of one wall, as

seen in Fig. 5.1. The door is 0.8 m wide for the over-ventilated fire and 0.2 m wide for the under-ventilated condition. The room is built using sheet steel and two layers of insulation applied on all sides, top and bottom in the form of ceramic fibre blanket. The pool fire is square consisting of C_7H_{16} with an area of 1 m^2 for the over-ventilated case and 0.5 m^2 for the under-ventilated fire. A pump-feed burner controls the MLR for the over-ventilated case. An open pan with a fixed amount of fuel is placed for the under-ventilated case and the MLR measured. The door remains fully open for the duration of the tests [38].

Two water-cooled species probes and two type-R thermocouples are placed in two locations at a near ceiling level as seen in Fig. 5.1. The first location (T_1, Probe 1) is between the pool and the back wall, the second (T_2, Probe 2) is between the pool and the door. O_2 as well as combustion products carbon dioxide (CO_2) and CO are measured. A large-scale calorimeter is set up to calculate the HRR based upon the O_2 calorimetry principle.

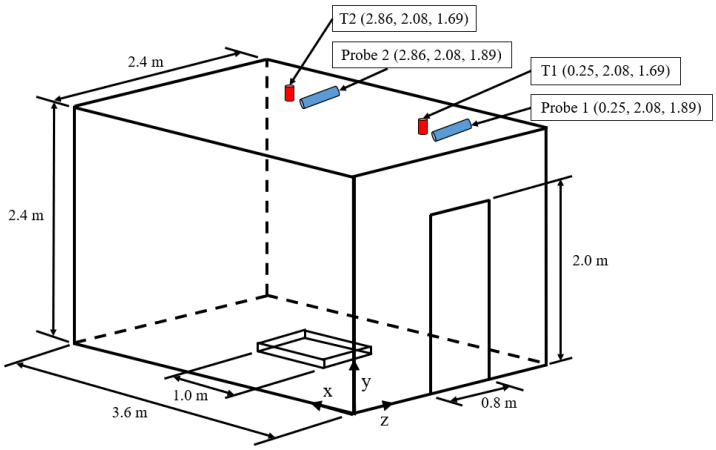

Figure 5.1: Schematic of the room setup and measurement locations (shown in brackets) for the over-ventilated case; reproduced from [38]. All dimensions in meters.

5.2 Chemistry

Combustion is modelled using a partially stirred reactor (PaSR) approach. In contrast to most fire models [54], this approach considers a finite rate instead of the infinitely fast approach, as in the EDC model. In EDC, when fuel and oxidizer are sufficiently mixed, the mixture is "burnt" with the reaction taking place instantaneously. The Damköhler number

($Da = \frac{\tau_t}{\tau_c}$) is assumed to be much larger than unity. Therefore, the chemical time scale τ_c is much smaller than the flow time scale τ_t [23]. However, the reaction rate calculated in the PaSR approach is based on both the turbulent and chemistry time scales.

In the present work, a two-step reaction mechanism is applied, as shown in Table 5.1. This is a simplification, as in reality many intermediate steps take place [85]. The balanced first reaction is presented in Table 5.1 and produces CO and water vapour (H_2O). The second equation is the oxidation of CO to CO_2. Nitrogen (N_2) is present but inert in both reactions. These reactions use finite chemistry based upon the Arrhenius chemical reaction rate and specified coefficients. These coefficients are specified in Table 5.1. The result is a fast first reaction and a slower second reaction. A chemistry solver is needed to calculate the rate constant, k. Soot production is neglected in the present study, as the available soot model does not influence the thermodynamics of the system [1].

Table 5.1: Reaction rate constants to calculate $k = A\ exp(-E/RT)$, where A is the pre-exponential coefficient, E is the activation energy, R is the universal gas constant, T is temperature, and m and n denote the order of reaction corresponding to the first and second reactant species, respectively. [31, 78, 85].

Reaction	A [cm^3/mol s]	E [J/mol]	m	n
$C_7H_{16} + 7.5O_2 \rightarrow 7CO + 8H_2O$	6.3×10^{11}	125 520	0.25	1.5
$CO + 0.5O_2 \rightarrow CO_2$	2.53×10^{12}	199 547	1	0.25

5.3 Numerical Implementation

The computational domain is defined according to the geometry of the room, discretized, thermophysical properties tabulated, model settings selected, and boundary conditions applied. An extended domain is added to the computational domain outside the door, as seen in Fig. 5.2. The fuel inlet can be seen inside the compartment with the 'air box' on the exterior of the thin door. The boundaries at the extent of the air box are set to be pressure driven velocity conditions, where they can act as an inlet or outlet at any point depending upon the calculated pressure. The walls, ceiling, and ground are set to a no slip condition for velocity and zero gradient for most other properties. The pool fire is modelled as a mass flow rate inlet condition, where the flow is C_7H_{16} vapour at an elevated temperature to initiate combustion (T=1000 K). The experimentally measured MLR is set

as the input to the simulations. FvDOM is again selected for the radiation model. For C_7H_{16} pool fires, a value of 0.33 for χ_r is found to be a good approximation for diameters ranging up to 2 m in size [35]. These simulations also employ the k-equation eddy viscosity model. The PIMPLE algorithm is applied and first order discretization is selected. Spatial

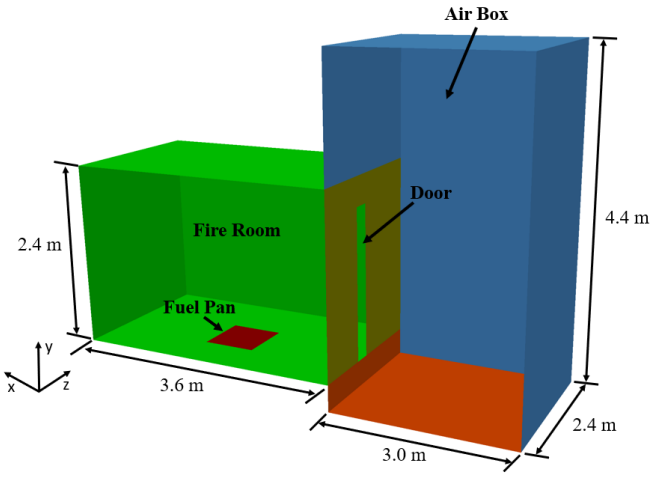

Figure 5.2: Schematic of computational domain (under-ventilated case).

schemes are all second order accurate. A maximum Courant number of 0.8 is enforced and the time step initially set to 0.001 s and allowed to vary according to the Courant number limit.

5.4 Sensitivity Analysis

Before the numerical results are discussed, a grid analysis is explored. Two main techniques are applied; a mesh independence study and a non-dimensional number check of grid size in relation to HRR. Further, a sensitivity analysis is conducted to determine the impact of varying a sub-model parameters related to the turbulence, combustion, and radiation approaches.

5.4.1 Mesh Sensitivity

Three mesh sizes are created, of approximately 200 000, 600 000, and 850 000 cells. Refinement is added in the flame region due to the predicted large gradients in velocity and

temperature values. Temperatures are compared due to best representing how the mesh effects the results and are of similar magnitude or greater than other flow values such as velocity or species concentrations. The magnitude of maximum temperature difference is 3% between the 600 000 mesh and 850 000 mesh, as calculated from 5.3. An additional

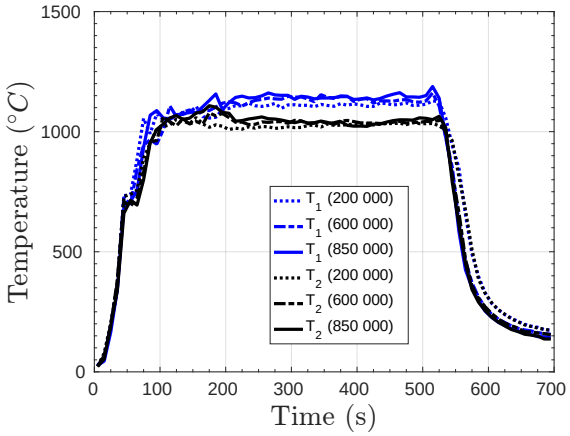

Figure 5.3: Temperature sensitivity comparison on three different mesh densities.

mesh resolution criterion, based on the characteristic fire diameter (D^*) and the average cell side length ($\overline{\Delta}$), is tested. According to McGrattan et al. [53] if $D^*/\overline{\Delta} > 10$, as calculated from Eq. 5.1, the mesh is sufficiently resolved. As defined by Bounagui et al. [18], D^* is based upon the fire size by including the total HRR ($\dot{Q}$), properties of the fuel, and ambient conditions.

$$D^* = \left(\frac{\dot{Q}}{\rho_\infty T_\infty c_p \sqrt{g}}\right)^{2/5}. \tag{5.1}$$

In the present study, an average cell size in the compartment of 3.5 cm is calculated from the 600 000 cell mesh which corresponds to a $D^*/\overline{\Delta}$ value of 30, which satisfies the criteria. Hence, the 600 000 cell mesh is selected which has a relatively uniform density of 4.2 cm side length in the compartment, refined to 2.1 cm in the flame region. This mesh density is within the range of other pool fire models. Hwang et al. [38] had an average spacing of 5 cm and a total cell amount of 600 000. Wang et al. [84] refined the mesh to 1.25 cm spacing in the flame region when looking solely at a pool fire. Lazaro et al. [47] completed compartment fire simulations with a uniform mesh spacing of 5 cm. Cai and Chow [20] found a mesh of 400 000 cells to be mesh independent in their LES simulations of an octane pool fire in a compartment of the same size investigated here.

5.4.2 Numerical Parameter Sensitivity

A study is performed to determine the magnitude of effect of a few main sub-model implementation. These include the effect of implementing two-step chemistry on the under-ventilated case, the effect of a varying the constants in the SGS formulation, the number of radiation divisions in the fvDOM implementation, and the effect of varying the constants in the SGS formulation.

Chemistry

The effect of the two-step chemistry implementation is investigated compared to a one-step reaction. As expected, a significant difference in the product species concentration is found. In the one-step mechanism shown in Eq. 5.2, no CO is produced, while in the two-step a maximum concentration of 0.046 is found. As seen in Fig. 5.4 the difference in CO_2 concentration (x_{CO_2}) is significant. During the steady state phase of 200–500 s, an average CO_2 concentration is 0.15 with one-step decreasing to 0.10 volume fraction with two-step. The difference in the profile of O_2 concentration is minimal between the mechanisms. Temperature is shown in Fig. 5.5. Similar profiles are observed during the growth phase, then the two-step reaction predicts a 5% lower temperature through the steady state and decay region.

$$C_7H_{16} + 11O_2 \rightarrow 7CO_2 + 8H_2O \tag{5.2}$$

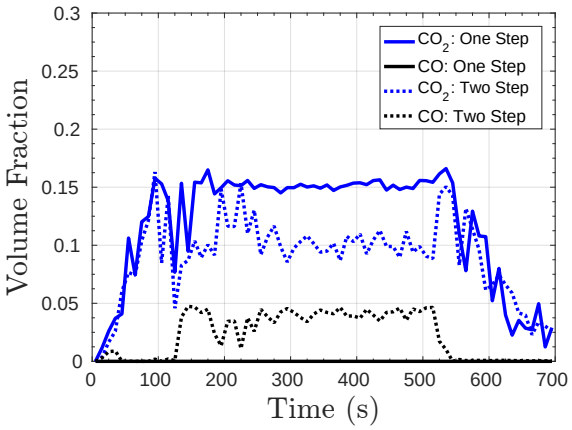

Figure 5.4: Combustion product concentrations at Probe 1.

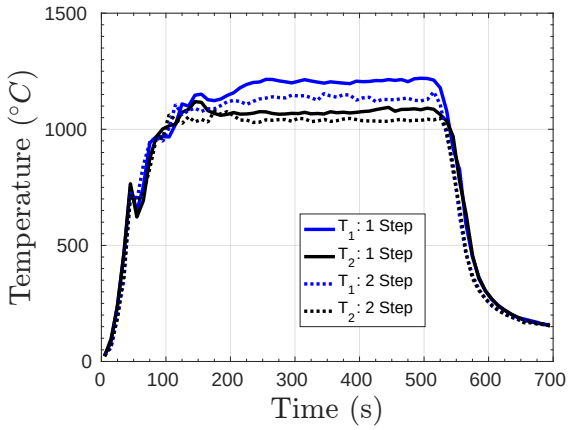

Figure 5.5: Transient temperatures at Probe 1.

FvDOM Discretization

The effect of the number of solid angles (ϕ) along which the RTE is solved is examined. The higher the amount angles, the higher the accuracy of results. As suggested by Chatterjee

et al. [21], 48 angles are usually sufficient to adequately resolve the radiation within the fire. When heat flux is of interest, outside the fire, up to 96 angles may be required. In this study, minimal effects on the temperature and species concentrations are found between the angular discretization. The temperature results varying by less than 2% through the steady state region across 16, 64, and 96 solid angles. Similar differences are found in species concentrations, in that they show less than 2% difference between 64 and 96 solid angles. In addition to the steady state results, the comparison of transient profiles had differences similar in magnitude. An amount of 64 angles is specified and determined to be appropriate for this study as it does not significantly increase computational time while still solving the RTE across an adequate amounts of angles.

SGS Constants

As outlined in Eqs. 4.10–4.12, a one equation SGS model with constant coefficients is implemented. Different values of the constant C_k can be specified. Yoshizawa [87] recommended 0.05 as the default value when creating the model. However, in fireFOAM, defaults of 0.06 and 0.07 have been set, depending on the release version [32]. The magnitude of these differences at Location 1 are shown in Table 5.2 for the under-ventilated case. The largest difference is in the O_2 concentration, where the concentration is 0.12×10^{-3} for C_k=0.05 and negligible for both C_k=0.06 and C_k=0.07. For the temperature and remaining species, the largest differences are on the order of 5%. Therefore, the results are fairly insensitive to the SGS model constants investigated and a C_k of 0.05 is selected for further results due to the original author recommendation [87].

Table 5.2: SGS constant comparison during steady state period (200–500 s) of under-ventilated fire.

	C_k=0.05	C_k=0.06	C_k=0.07
T $(°C)$	1129	1135	1137
$x_{0_2}(10^3)$	0.120	0.000	0.001
x_{CO_2}	0.103	0.105	0.105
x_{CO}	0.041	0.039	0.038

5.5 Results

Predictions of temperature and species concentrations are presented for the over-ventilated case and the under-ventilated case. For each case, the modelled vs. ideal HRR is shown. The ideal HRR is the measured MLR (the input to the model) multiplied by the heat of combustion of C_7H_{16}. The temperature and species results are compared to the experimental measured values. Finally, a comparison is made to the previous numerical results performed in FDS [38].

5.5.1 Comparison with Experiment - Over-ventilated Case

The predicted HRR is similar to the ideal HRR, as expected due to the well ventilated conditions which do not inhibit combustion efficiency. As shown in Table 5.3, the largest discrepancy is 22% during the early part of the burn. Good agreement is found ($< 3\%$ discrepancy) during the next two steady state periods, before increasing to 9.4% for the 400 s period of maximum HRR. The temperature predictions for the two measurement

Table 5.3: HRR during four steady state periods of the over-ventilated fire.

Time (s)	Exp. (kW)	LES (kW)	Difference (%)
800–1200	780	606	-22
1650–2050	1080	1105	+2.3
2400–2800	1680	1729	+2.9
3300–3700	2070	2265	+9.4

locations are presented in Fig. 5.6. As previously shown by the HRR, the growth of the fire is regulated by four periods of steady state heat release. The maximum temperature reached is 1378°C at T_1 and 1226°C at T_2. Temperature is well predicted by the model for the majority of the time between 1000 and 3000 s. After ignition ends, the temperature drops towards ambient in the computational domain at a faster rate than recorded in the experiments. Under-predictions of approximately 30% and 25% occur during the first and fourth steady state region, respectively. The 30% under-prediction in temperature, and 22% under-prediction in MLR, present from 800–1200 s, is due to no experimental MLR being measured over the initial 400 s. As the experimental MLR is the input to the LES simulation, combustion is delayed compared to the experiment. The species concentrations of O_2, CO_2, and CO are presented in Fig. 5.7 and Fig. 5.8, for Probe 1 and Probe 2,

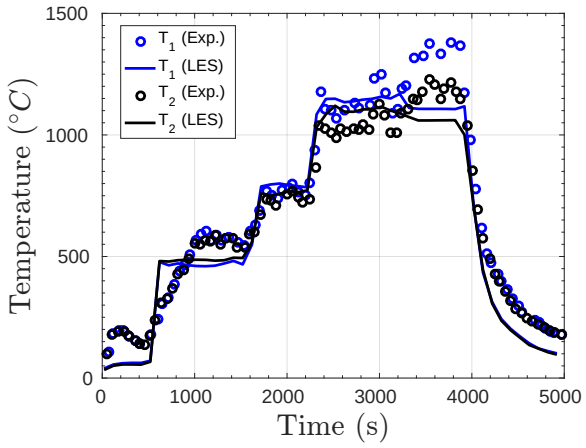

Figure 5.6: Over-ventilated transient temperatures.

respectively. The species probes are located in close proximity to the thermocouples, T_1 and T_2. The O_2 concentrations drop in step as the temperature increases, until reaching a minimum value of 0.02 in the experiment. However, the current simulations predict a minimum concentration of less than 10^{-5} at 3100 s, at Probe 2. The O_2 concentration then fluctuates between 0.04 and 10^{-4} until 3950 s, at which point the concentration rises back towards ambient concentration. The predicted O_2 concentrations at Probe 1 are in closer agreement with the transient profile of the experiment, except reaching negligible amounts ($< 10^{-4}$) at some points between 3300–3900 s. In general, O_2 volume fractions are under-predicted by an average of 15% throughout the burn. When combustion ends the simulation predicts a return to ambient O_2 concentrations (20.5%) at a similar rate to that observed in the experiment. Correspondingly, the CO_2 concentration increases as the O_2 concentration decreases, to a maximum volume fraction of 0.11 in the experimental case. Maximum volume fractions of 0.14 and 0.16 are predicted at Probe 1 and Probe 2, respectively. Since the O_2 concentration is under-predicted it follows that the CO_2 concentration is over-predicted by a similar amount. This is shown in Fig. 5.8 near the 2100 s mark where O_2 concentration is under-predicted by a volume fraction of 0.04 and the CO_2 concentration is over-predicted by a volume fraction of 0.04. For the remainder of the burn duration the predictions are in good agreement. Since O_2 is always present in the compartment, minimal amounts of CO are produced. Maximum experimentally observed values are 0.014 and 0.006 CO concentrations at Probe 1 and Probe 2, respectively. However, since the simulations predict O_2 depletion for a brief time, the CO concentration reaches 0.072 and

0.061 at Probe 1 and Probe 2, respectively. The indication from these species predictions is that the modelled reaction rate is higher than what is observed experimentally due to the over-consumption of O_2 and increased combustion product concentrations. This is consistent with the over-prediction of up to 10% in the modelled HRR. A visualization

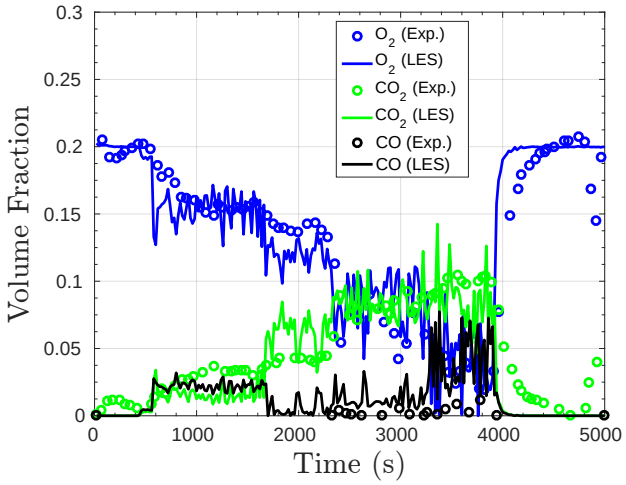

Figure 5.7: Over-ventilated species concentrations at Location 1.

of the flow domain is shown in Fig. 5.9. The temperature contours are plotted as a slice through the middle of the compartment illustrating the fire plume and developing hot layer. Velocity vectors are presented, scaled to their velocity magnitude. The flow field shifts the fire plume towards the rear of the compartment, resulting in slightly higher temperatures at T_1. The neutral plane is observed approximately halfway up the height of the doorway. The incoming ambient air enters in the lower half and the hot fire gases exit in the upper half due to buoyancy effects.

5.5.2 Comparison with Experiment - Under-ventilated Case

The key difference in the under-ventilated room is the lack of O_2 due to the narrow door opening and resultant incomplete combustion that occurs. Since the room is under-ventilated, the combustion efficiency is predicted to decrease and not release the full heat amount of the fuel. During the under-ventilated burn, there is growth up until an approximately steady state window from 200–500 s, as seen in Fig. 5.10. During this time frame, the experimentally measured HRR is 1480 kW. This is significantly less than the

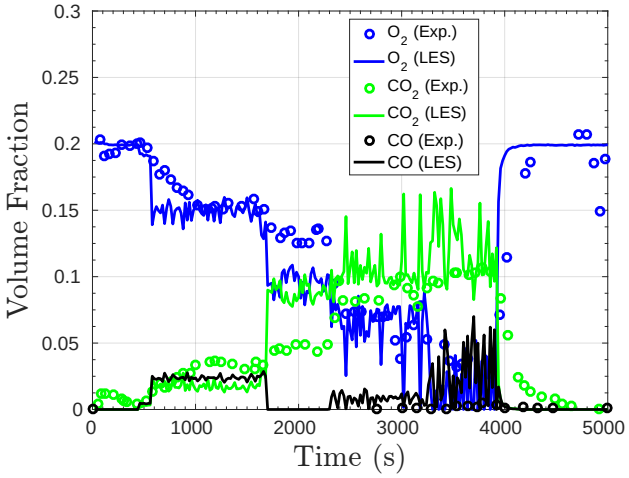

Figure 5.8: Over-ventilated species concentrations at Location 2.

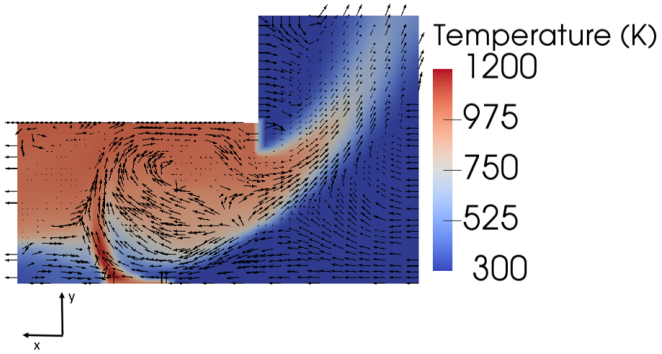

Figure 5.9: Temperature contour slice with velocity vectors at cross section of domain.

ideal HRR of 1830 kW for complete combustion. The reason for this discrepancy is the under-ventilated conditions reduce the combustion efficiency. The modelled HRR is in good agreement with capturing the reduction in efficiency, as a value of 1532 kW as predicted, a difference of +3.5% from the measured HRR. This is consistent with the slight over-prediction in the over-ventilated case.

A rapid temperature increase occurs over the first 100 s, as seen in Fig. 5.10, until reaching approximately 1000°C. The fire then becomes relatively steady state (200–500 s), increasing to a maximum temperature of 1269°C at T_1 and 1162°C at T_2 in the experi-

mental case. The fuel is fully consumed and the temperatures decrease towards ambient after 500 s. Near the end of the growth period the model slightly over-predicts temperatures by an average of 61.3°C between both locations, and under-predicts the peak temperatures by 84.0°C. After burning ends the temperatures in the model drops at a more rapid rate towards ambient than experimentally measured. This discrepancy is likely due to not accounting for the heat retained by the walls in the simulations which re-emits a significant amount of energy in the experimental case. The impact of the narrow door

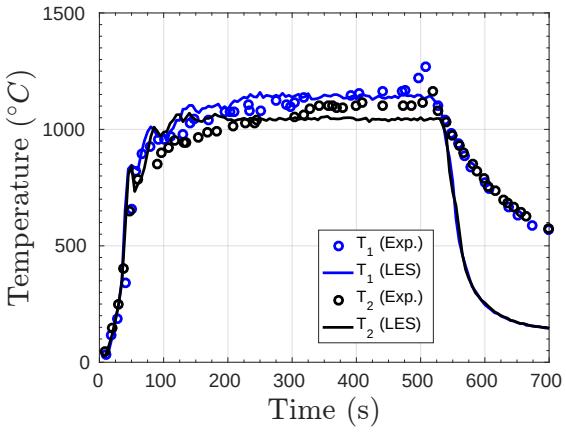

Figure 5.10: Under-ventilated transient temperatures.

width and resultant under-ventilated nature of the fire can be clearly seen from the species concentrations of Fig. 5.11 and Fig. 5.12. O_2 concentration drops rapidly, and reaches a negligible amount approximately 100 s after ignition. This corresponds to the leveling off of temperature due to the reduced combustion efficiency of the O_2 depleted environment. The O_2 concentration is predicted well, lagging behind slightly in its consumption, by 20 s during the growth phase. As expected, the experimental CO_2 concentration increases until approximately 100 s where it levels off below 10% for the majority of the steady state. The predicted CO_2 concentrations show good agreement during the growth phase of the fire, but are over-predicted by an average of 55% at Probe 2 and 37% at Probe 1 during the steady state phase. The predicted decrease of CO_2 during the decay phase lags behind the experimental results by 40 s. CO is present in significant amounts due to the under-ventilated nature of this test case. At the end of the steady state burning region, the experimental CO concentration is at a maximum of 0.06. The CO concentrations are

well predicted with a brief over-prediction during the end of the growth phase. During the steady burning phase, an over-prediction of 2.0% is found at Probe 1, and an under-prediction of 13.9% at Probe 2. The better agreement found in the under-ventilated case is due the limitation of the reaction rate on the O_2 concentration and less reliant on the specific constants selected in the two-step mechanism.

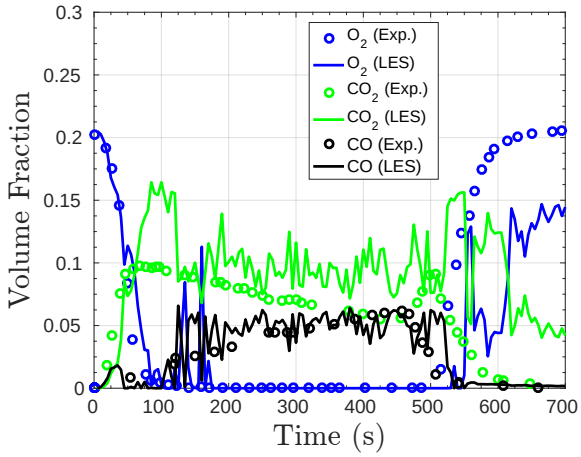

Figure 5.11: Under-ventilated species concentrations at Location 1.

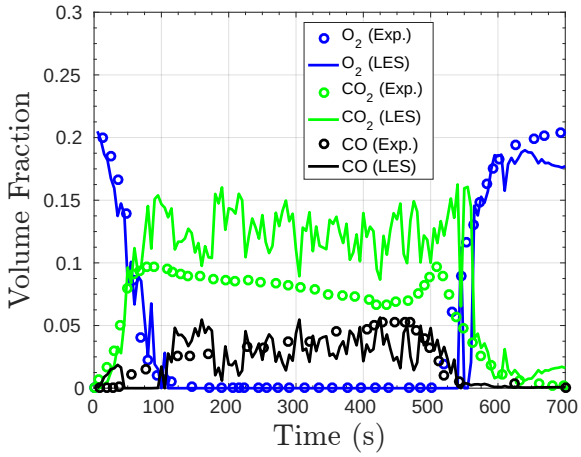

Figure 5.12: Under-ventilated species concentrations at Location 2.

5.5.3 Comparison with Previously Published Numerical Predictions

A comparison is made between these predictions made in fireFOAM with previously published predictions made in FDS [38]. FDS 5 is used, with many similarities of the formulation and implementation as in fireFOAM including the low-Mach number derivation of the governing equations, fvDOM radiation model, and second order accurate discretization schemes in time and space. The main differences are that the previous results:

- Implement a constant Smagorinsky SGS model (C_s=0.2) [51]
- Utilize a three parameter mixture fraction combustion model, with prescribed soot yield
- Implement a turbulent Prandtl number of 0.5 compared to a value of 1 in the current study
- Do not account for radiative scatter of gaseous species

Both the Prandtl number difference and lack of radiative scatter are found to have a negligible impact on the temperature and species predictions. By modifying the Prandtl

number to 0.5, in the current under-ventilated simulations, less than a 1% difference is found for temperatures and most species. In the case of O_2, up to a 4% difference is found, however this is at very low concentrations. Therefore, the two significant differences between the simulations are the SGS model and combustion model.

A subset of the experimental, current, and previous results are presented in Table 5.4 for the over-ventilated case. Two sets of data for the rear sampling locations (Probe 1) are time averaged during two steady burning periods. The first period, corresponding to an experimental HRR of 1080 kW shows a slight over-prediction of temperature (9.2%) in the current work and an under-prediction of a similar magnitude (8.2%) by the previous results. The O_2 concentration is under-predicted in both cases, by 12.2% in the current case and 8.6% in the previous case. CO_2 concentration predictions are well predicted in the previous results, whereas the CO_2 concentration is over-predicted in the current study. As the case is over-ventilated, low concentrations of CO are predicted. CO concentration is well predicted by the current results and over-predicted by the previous results.

For the period of steady burning at maximum HRR, shown in Table 5.5, the current results under-predict temperature by 13.2%, while the previous results are in good agreement. This under-prediction is caused by reaching under-ventilated conditions for a brief time at the start of the steady state period. The averaged O_2 concentration is slightly over-predicted (14%) in the current case, and more-so in the previous case (44%). CO_2 concentration is under-predicted by a similar small magnitude in both sets of simulations. Relatively good predictions are found for CO concentration in the previous results, but over-predicted significantly in the current study. The elevated CO concentration is due to the period of under-ventilation predicted in the current simulations.

Table 5.4: Averaged values of temperatures (T_1) and species for period of steady burning, 1650–2050 s.

	Experimental	Current	Previous
T $(°C)$	740 ($\pm$44)	808	679
x_{O_2}	0.139 ($\pm$0.016)	0.122	0.127
x_{CO_2}	0.042 ($\pm$0.005)	0.059	0.043
x_{CO} (10^3)	0.20 ($\pm$0.02)	7.70	5.50

A similar comparison is made with the under-ventilated results, which are time averaged between 200–500 s, and shown in Table 5.6. Excellent agreement in temperature is found in the current study, with an under-prediction of 6.6% in the previous case. O_2

Table 5.5: Averaged values of temperatures (T_1) and species for period of steady burning, 3300–3700 s.

	Experimental	Current	Previous
T $(°C)$	1310 ($\pm$79)	1137	1305
x_{O_2}	0.036 ($\pm$0.004)	0.041	0.052
x_{CO_2}	0.099 ($\pm$0.012)	0.087	0.088
x_{CO} (10^3)	4.80 ($\pm$0.58)	41	5.2

is under-predicted currently and over-predicted in the previous case. However, the very low concentrations predicted in both cases agrees with the experimental results. CO_2 is correspondingly over-predicted currently (38%) and in the previous case (19%), to a lesser extent. CO predictions are within 5% agreement in both sets of simulations.

Table 5.6: Temperature (T_1) and species comparison during steady state period (200–500 s) of under-ventilated fire.

	Experimental	Current	Previous
T $(°C)$	1130 ($\pm$68)	1140	1055
$x_{0_2}(10^3)$	0.448 ($\pm$0.054)	0.00	1.51
x_{CO_2}	0.069 ($\pm$0.008)	0.095	0.082
x_{CO}	0.050 ($\pm$0.006)	0.051	0.048

5.6 Conclusions

A compartment fire simulation within fireFOAM is completed and compared to two differently ventilated experimental cases. The simulation includes the thermal effects of the walls and a simulated 'air box' where the domain outside the door is extended to reduce the effect of the boundaries and better capture the flow behaviour within the room. A two-step chemistry mechanism is implemented and combined with the PaSR combustion model, instead of the commonly selected EDC and associated infinitely fast chemistry assumption. A sensitivity study is performed to determine the effect of three criteria critical to the sub-modelling efforts:

- Two-step chemistry is necessary for under-ventilated fires to accurately predict species concentrations, but does not significantly affect the temperature predictions
- 64 rays are sufficient for the implementation of the fvDOM radiation model and pose an acceptable compromise between accuracy and computational cost
- Varying the k-equation SGS constant between 0.05-0.07 has a small effect on the predictions

Temperatures are well predicted throughout both cases, with an under-prediction at peak HRR in the over-ventilated case. This is due to a brief period of predicted low O_2 concentration which inhibits the combustion efficiency. For the over-ventilated test, the O_2 predictions are low, and CO_2 concentration predictions are high by a similar magnitude. O_2 and CO is well predicted in the under-ventilated case, with periods of over-prediction of CO_2. It is concluded that the models reaction rates are too fast. Modifying the reaction rate constants could address this issue. The numerical results are similar in magnitude of agreement with the experimental results, when compared to a set of previous results which applied different combustion and SGS models.

Chapter 6

Multi-Compartment Fire Modelling

The objective of the present chapter is to extend the simulations performed in Chapter 4 and Chapter 5, to investigate the heat transfer into and through a solid wall section. This chapter serves as a preliminary study into conjugate heat transfer. The experimental set-up is defined, and a non-degrading wall selected for the present study. The numerical approach is detailed with the added complexity associated with the selected experiment. Thermal comparisons are made with the experimental results focusing on the effects of the wall section. Finally, improvements are proposed to further expand the simulations to include degrading wall sections.

6.1 Experimental Details

The experimental domain consists of a shipping container modified to accommodate a wall dividing the container into two sections. The front section is the fire compartment, with a 0.8 m wide door centered in one wall. The back section is isolated from the fire by a steel frame in which a wall section is placed. A representation of this setup is shown in Fig. 6.2. The compartment measures a total of 4.7 m x 2.4 m x 2.3 m. The wall section is 0.3 m smaller on each side compared to the cross-sectional dimensions of the compartment, due to the steel frame [27].

A total of 17 experimental tests were performed. These tests were separated into two categories, 12 performed with a non-degrading steel wall section and 5 performed with various degrading wall sections. The degrading walls consist of representative materials, including wood studs, insulation, and gypsum board. A non-degrading test case is selected

for the present study. The fuel load for this test consists of four crib fires (Crib 1 = 14.13 kg, Crib 2 = 15.14 kg, Crib 3 = 15.21 kg, Crib 4 = 15.07 kg), and a small CH_3OH pool, placed under Crib 1 to facilitate ignition. These cribs are all approximately 15 kg. The door is partially blocked by an obstruction placed at an angle of 15 degrees from vertical, seen in Figure 6.1, therefore blocking most of the door. The perimeter walls of the compartments are insulated, and the dividing wall section is steel. The test is conducted for 90 min, during which time the ignition of each crib is recorded as well as temperatures throughout the domain. Instrumentation consists of several thermocouple rakes located

Figure 6.1: Obstruction angled at 15 degrees in front of the single opening; taken from [27].

in different areas, and attached to the unexposed side of the wall section. In the present study, a subset of the thermocouple readings are selected for comparison. The selected thermocouples are shown in Figure 6.2 as T_1-T_6. T_1 and T_2 are in the fire compartment, at heights of 2.2 m and 0.3 m, respectively. T_3 and T_4 are affixed to the unexposed side of the steel wall at heights of 2.05 m and 0.45 m, respectively. T_5 and T_6 are in the isolated room at heights of 2.2 m and 0.3 m, respectively.

6.2 Numerical Implementation

The numerical implementation for this study is similar to that outlined in Chapter 4. These similarities include one-step chemistry with the EDC combustion model, the k-equation for

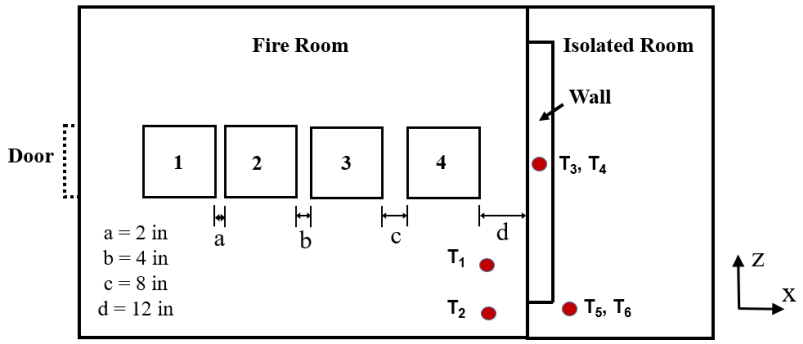

Figure 6.2: Instrumentation and fuel load for test selected for present study.

SGS turbulence closure, the fvDOM approach for radiation, and the PIMPLE algorithm for the numerical solution procedure. A maximum Courant number of 0.8 is again enforced with first order temporal discretization and second order spatial discretization. Since the steel wall is within the domain of interest, both sides of this wall have the same boundary condition as applied in Chapters 4 and 5, accounting for radiation and convection heat transfer.

The main differences in the simulations from Chapter 4 are the geometry, material properties, and fire conditions. The computational domain is shown in Fig. 6.3. The door in the simulation is 0.14 m wide, compared to 0.8 m in the experiment. This is to account for the reduced opening area caused by the physical obstruction in the experiment, seen in Fig. 6.1. The four crib locations can be seen along the majority of the length of the fire compartment. The thermophysical properties of the materials of interest are shown in Table 6.1. The boundary conditions are ambient pressure (P = 985 700 Pa)

Table 6.1: Thermophysical properties of the walls [3, 10, 14, 89].

Property	Steel	Insulation
k ($\mathrm{Wm^{-1}K^{-1}}$)	42	0.05
ρ ($\mathrm{kgm^{-3}}$)	7850	94
c_p ($\mathrm{Jkg^{-1}K^{-1}}$)	487	1130
ϵ	0.75	0.85

and temperature (T = 25.2°C) with zero gradient conditions specified for velocity and

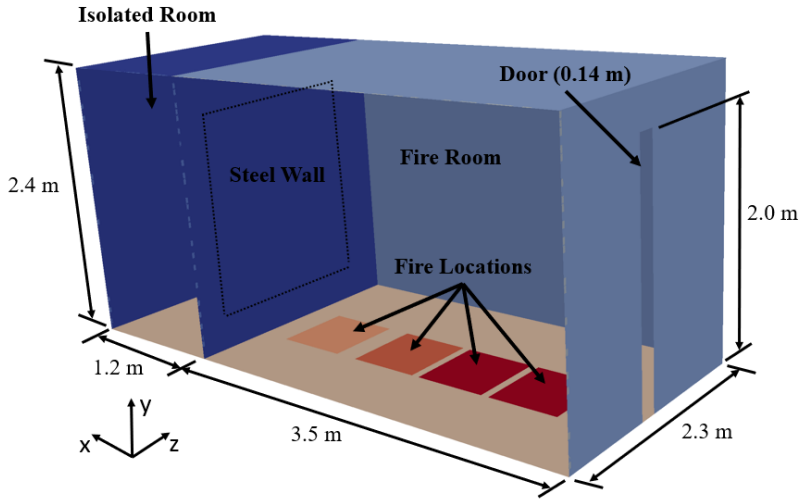

Figure 6.3: Computational domain.

species concentrations. For the fire, a simplification in the current numerical case is made to represent the wood cribs as CH_3OH pools. Pyrolysis is not included in the current simulations, therefore a MLR of CH_3OH is specified to produce an equivalent HRR as what is produced by the experimental wood cribs. The timing of ignition for each crib is experimentally measured, then an HRR curve constructed based upon the mass of each crib and the heat of combustion of wood ($\Delta H_c = 14\ 800$ kJ/kg) [28]. The HRR for each crib is then divided by the heat of combustion of CH_3OH ($\Delta H_c = 725$ kJ/mol) to determine the MLR for each fire location, which is then a boundary condition to the simulations.

Mesh independence is confirmed and a final mesh of 600 000 cells is selected. This mesh corresponds to cells with a side length of 6.5 cm, which are refined to a side length of 3.3 cm in the flame regions.

6.3 Results

The simulated HRR is first compared to the experimental HRR to ensure an accurate reflection of the fire conditions. The predicted HRR is shown in Fig. 6.4. The total HRR from all four crib locations increases until 1800 s, reaching a value of 719 kW in the experimental case and 750 kW in the simulation. The HRR decays over the next 1200 s until the fuel is exhausted. The simulated HRR shows good agreement to the experimental values with over-predictions of less than 5% at the maximum HRR. Figure 6.5 shows the

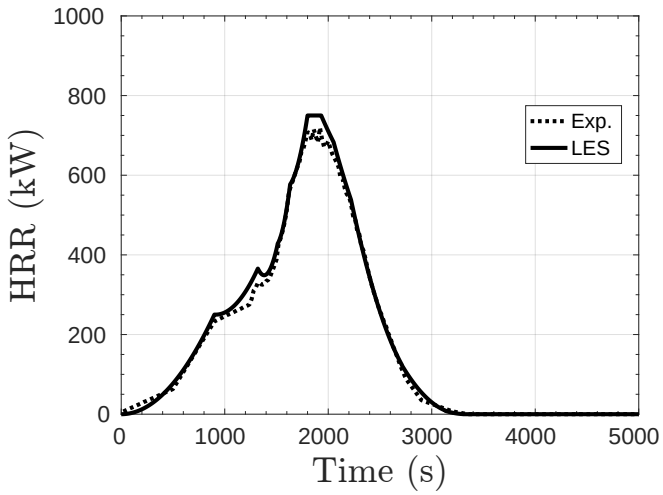

Figure 6.4: Simulated HRR vs. experimental HRR.

temperatures at two locations (T_1 and T_2) in the rear corner of the fire compartment. T_1 reaches a maximum experimental temperature of 686°C at 1931 s and T_2 reaches 324°C at 2530 s. These experimental temperatures remain approximately constant for 700 s before starting to decrease due to the reduced HRR from the cribs. The simulation well predicts the transient T_1 profile with good agreement during the growth phase of the fire. An over-prediction of 125°C occurs at the maximum HRR. T_2 is over-predicted during the growth phase and then decays 600 s earlier than experimentally recorded. This discrepancy is likely due to the inaccuracy in modelling the physical obstruction. As seen in Fig. 6.1, the bottom of the door is heavily obstructed, whereas the top has a higher area for air to flow. In the simulations, the door is uniform in width. Therefore, the simulations predict a higher amount of airflow in the lower section of the door than is realistic. At lower heights in the door, below the neutral plane, incoming air enters. As this air is at a low temperature compared to the fire gases, the predicted temperatures cool down faster than the experimental temperatures.

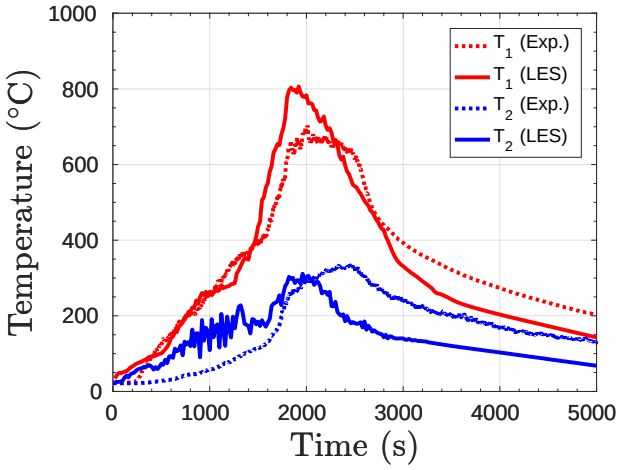

Figure 6.5: Temperatures in corner of fire compartment at heights of T_1=2.2 m and T_2=0.3 m.

The wall temperatures are shown in Fig. 6.6, where T_3 is at a height of 2.02 m and T_4 is at a height of 0.45 m. Due to the high conductivity of the steel, similar magnitudes at both locations are observed. The largest discrepancy between the experimental T_3 and T_4 is 92°C and the difference becomes negligible during the decay phase of the fire when the heat has time to equalize throughout the steel. The simulations well predict the temperatures during the growth phase, however under-predict significantly at the maximum HRR. A possible cause for the under-prediction is the emissivity value of steel. Emissivity governs the amount of radiant energy absorbed and emitted by a surface, which has a significant effect on temperature in fire scenarios. A range of emissivity values is possible depending upon the surface finish of the material.

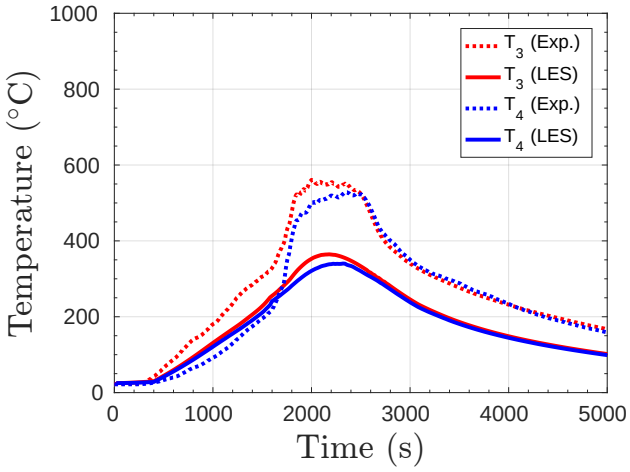

Figure 6.6: Temperatures on unexposed side of steel wall at heights of T_3=2.05 m and T_4=0.45 m.

Figure 6.7 shows two temperatures in the isolated compartment. The temperature increases are a result of heat transfer through the steel wall. In the experiments, a division is seen between the upper layer and the lower layer with T_5 reaching 211°C and T_6 reaching 114°C. The numerical predictions show a much lower separation in temperature. T_5 is well predicted, but T_6 is over-predicted significantly. Since the wall temperatures are under-predicted it is evident that too much heat is being transferred through the wall into the isolated compartment. During the decay phase, the predicted temperatures decrease at a faster rate than the experiments.

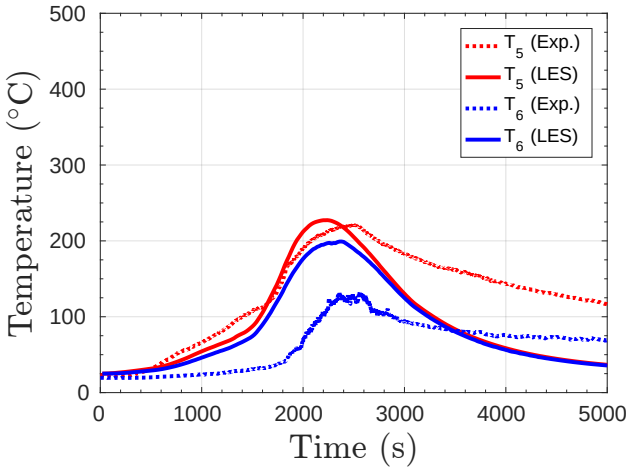

Figure 6.7: Temperatures in isolated compartment heights of T_5=2.2 m and T_6=0.3 m.

6.4 Conclusions

In this chapter, the simulations are extended to include a secondary compartment separated by a wall section. A simplification is made to model the wood cribs as CH_3OH pool fires, to reduce the complexity and uncertainty related to pyrolysis modelling. Numerical predictions are compared with an experimental case investigating a non-degrading wall section. Temperature trends are well predicted in the fire compartment. Wall temperatures are under-predicted due to the large amount of heat transfer through the wall. Consequently, the isolated compartment temperatures are slightly over-predicted. During the decay phase, predicted temperatures drop faster than those in the experiment. This decrease is due to modelling the door obstruction as a uniform reduced width. These simulations can be used as a first step toward investigating degrading wall sections, if pyrolysis modelling is implemented.

Chapter 7

Conclusions

A series of numerical investigations are conducted into common fire experiments, primarily using the fireFOAM CFD software. Good predictions of temperatures and species concentrations are obtained as compared to experimental results.

One fire experiment, the cone calorimeter is modelled using two approaches in Chapter 3, a finite difference formulation and CFD simulations. For the finite difference formulation, the energy balance method is applied to calculate the thermal response of a multi-layer specimen to a irradiance from the cone heater. Good agreement of the predictions is found compared to the experimental results, with some discrepancies due to uncertainty in the material properties of the insulation layer at elevated temperatures. Good agreement is again found in the CFD simulations, with an under-prediction at the centreline and over-prediction at the outer edge locations. This is due to the representation of the cone heater in the computational domain as a flat disc, therefore not reflecting the exact geometry of the heater and the resultant radial heat flux profile. In Chapter 4, the CFD simulations are extended to include a full-scale compartment fire test. LES is selected as the turbulence approach with a k-equation SGS model. Complete combustion and infinitely fast chemistry is assumed for the CH_3OH pool fire. Good agreement in temperature values is found at steady state, and prediction of the velocity exchange through the door matches the experimentally observed neutral plane height. In Chapter 5, a more complex fuel, C_7H_{16}, and under-ventilated compartment conditions are investigated. Within the CFD simulations, a two-step reaction mechanism is implemented, and shown to be necessary due to the significant amount of CO produced. Hence, finite rate chemistry and the PaSR combustion model are required where reaction rates are no longer assumed to be infinitely fast. The effect of SGS model constants are found to be minimal for the range of values selected. Predictions of temperature and species are well predicted, with an over-prediction

of CO_2 during the burning period, due to modelling the reaction rate too fast. Comparable agreement to experimental values is found to previous conducted LES results. Differences are attributed to the SGS model and combustion model. Finally, in Chapter 6, the CFD simulation involves heat transfer through a wall section into a separate compartment. A non-degrading steel wall is investigated in the present work, since pyrolysis is not implemented. Temperatures are under-predicted in the wall section, and over-predicted in the rear compartment, due to too much heat being transferred through the wall. This work can be used as a starting point to include treatment of pyrolysis and the ability to model degrading walls when exposed to fire.

Future work entails expanding the capabilities of the simulations developed by including pyrolysis modelling. For materials such as gypsum board and insulation, the degradation of these materials is critical to capture. This will necessitate the inclusion of mass transport and chemical reaction phenomena. Specifically, the release of water from the gypsum and binders from the insulation. Additional challenges are the decomposing surface of the material undergoing pyrolysis and the convection at the surface as vapours are released.

To enhance the capabilities of the cone calorimeter simulations, a more accurate representation of the cone geometry is needed to match the exact heat flux irradiance radial profile. Future studies should be performed with materials with well known material properties especially at elevated temperatures.

References

[1] OpenFOAM C++ source code guide. http://www.openfoam.com/documentation/cpp-guide/html/index.html. Accessed: 2017-03-01.

[2] Emissivity Values for Common Materials. Infrared Services Inc., http://www.infrared-thermography.com/material-1.htm, 2000. Online; accessed 2016-09-09.

[3] Fiberfrax Durablanket S: Technical Data Sheet A1-004. Insulcon, http://www.insulcon.com/products/fibre-products/blankets/, 2009. Online; accessed 2016-09-09.

[4] C. Aire. Experimental and numerical modeling of heat transfer in wall assemblies. Master's thesis, University of Saskatchewan, 2014.

[5] G.E. Andrews and J. Ledger. Enclosed pool fires in low ventilation enclosures: Flame temperatures and global heat loss using gas analysis. *Fire Saf. Sci.*, 6:591–602, 2000.

[6] ANSYS Inc. ANSYS CFX 18.0, 2017.

[7] ANSYS Inc. ANSYS Fluent 18.0, 2017.

[8] ASTM. ASTM E119, Standard Test Methods for Fire Tests of Building Construction and Materials. *ASTM International*, West Conshohocken, PA, 2011.

[9] ASTM International. *ASTM E1354-16a, Standard Test Method for Heat and Visible Smoke Release Rates for Materials and Products Using an Oxygen Consumption Calorimeter*, West Conshohocken, PA, 2016.

[10] ASTM International. *ASTM-E3057-16, Standard Test Method for Measuring Heat Flux Using Directional Flame Thermometers with Advanced Data Analysis Techniques*, West Conshohocken, PA, 2016.

[11] ASTM International. *ASTM E2257-17 Standard Test Method for Room Fire Test of Wall and Ceiling Materials and Assemblies*, West Conshohocken, PA, 2017.

[12] V. Babrauskas and R.D. Peacock. Heat release rate: the single most important variable in fire hazard. *Fire Saf. J.*, 18(3):255–272, 1992.

[13] N. Benichou, M.A. Sultan, C. MacCallum, and J.K. Hum. Thermal properties of wood, gypsum and insulation at elevated temperatures. 2001.

[14] T.L. Bergman and F.P. Incropera. *Fundamentals of heat and mass transfer*. John Wiley & Sons, 2011.

[15] R. Booth. Grenfell tower: insulation was not certified for use with flammable cladding. *The Guardian*, 2017.

[16] P. Boulet, G. Parent, Z. Acem, A. Collin, M. Försth, N. Bal, G. Rein, and J. Torero. Radiation emission from a heating coil or a halogen lamp on a semitransparent sample. *Int. J. Therm. Sci.*, 77:223–232, 2014.

[17] P. Boulet, G. Parent, Z. Acem, T. Rogaume, T. Fateh, J. Zaida, and F. Richard. Characterization of the radiative exchanges when using a cone calorimeter for the study of the plywood pyrolysis. *Fire Saf. J.*, 51:53–60, 2012.

[18] A. Bounagui, N. Benichou, C. McCartney, and A. Kashef. Optimizing the grid size used in CFD simulations to evaluate fire safety in houses. In *3rd NRC Sympos. Computat. Fluid D.*, pages 1–8, 2003.

[19] J. Cadorin and J. Franssen. A tool to design steel elements submitted to compartment firesozone v2. part 1: pre-and post-flashover compartment fire model. *Fire Saf. J.*, 38(5):395–427, 2003.

[20] N. Cai and W. Chow. Numerical studies on heat release rate in room fire on liquid fuel under different ventilation factors. *Int. J. Chem. Eng.*, Article ID 910869, 2012.

[21] P. Chatterjee, Y. Wang, K.V. Meredith, and S.B. Dorofeev. Application of a subgrid soot-radiation model in the numerical simulation of a heptane pool fire. *Proc. Combust. Inst.*, 35(3):2573–2580, 2015.

[22] C. Chen, J.J. Riley, and P.A. McMurtry. A study of favre averaging in turbulent flows with chemical reaction. *Combust. Flame*, 87(3-4):257–277, 1991.

[23] Z. Chen, V.M. Reddy, S. Ruan, N.A.K. Doan, W.L. Roberts, and N. Swaminathan. Simulation of mild combustion using perfectly stirred reactor model. *Proc. Combust. Inst.*, 36(3):4279–4286, 2017.

[24] K. Choi. *3D Thermal Mapping of Cone Calorimeter Specimen and Development of a Heat Flux Mapping Procedure Utilizing an Infrared Camera*. PhD thesis, Worcester Polytechnic Institute, 2005.

[25] S.T. Craft. *CUWoodFrame—a heat and mass transfer model for light-frame wood floors exposed to fire*. PhD thesis, Carleton University, 2009.

[26] S.T. Craft, B. Isgor, G. Hadjisophocleous, and J.R. Mehaffey. Predicting the thermal response of gypsum board subjected to a constant heat flux. *Fire Mater.*, 32(6):333–355, 2008.

[27] M. Didomizio. *Experimental Study of Thermal Degradation of Fire Resisting Compartment Partitions in Fires*. PhD thesis, University of Waterloo, 2017.

[28] D. Drysdale. *An introduction to fire dynamics*. John Wiley & Sons, 2011.

[29] European Committee for Standardization, Brussels, Belgium. *EN 1995-1-2:2004 Eurocode 5 – Design of timber structures. Part 1-2: General – Structural fire design*, 2004.

[30] T. Fateh, F. Richard, and T. Rogaume. Modeling of the pyrolysis of plywood exposed to heat fluxes under cone calorimeter. *Fire Saf. Sci.*, 11:208–221, 2014.

[31] J.E. Floyd and K.B. McGrattan. Extending the mixture fraction concept to address under-ventilated fires. *Fire Safety Journal*, 44(3):291–300, 2009.

[32] FM Global. firefoam-dev, 2018.

[33] M.J.A. Gemaque and F.S. Costa. View factors of samples tested in cone and cylinder calorimeters. *J. Heat Transfer*, 134(9):094503–1–094503–5, 2012.

[34] K. Ghazi Wakili, E. Hugi, L. Wullschleger, and T.H. Frank. Gypsum board in fire-modeling and experimental validation. *J. Fire Sci.*, 25(3):267–282, 2007.

[35] A. Hamins, T. Kashiwagi, and R.R. Buch. Characteristics of pool fire burning. In *Fire resistance of industrial fluids*. ASTM International, 1996.

[36] History.com. Chicago fire of 1871, 2010.

[37] D. Hosser and V. Hohm. Application of a new model for the simulation of coupled heat transfer processes during fires to safety relevant objects in nuclear facilities. *Fire Saf. J.*, 62:144–160, 2013.

[38] C. Hwang, A. Lock, M. Bundy, E. Johnsson, and G.H. Ko. Studies on fire characteristics in over-and underventilated full-scale compartments. *J. Fire Sci.*, 28(5):459–486, 2010.

[39] M. Janssens. *Calorimetry*, pages 905–951. Springer New York, New York, NY, 2016.

[40] P.F. Johnson, V.R. Beck, and M. Horasan. Use of egress modelling in performance-based fire engineering design-a fire safety study at the national gallery of victoria. *Fire Saf. Sci.*, 4:669–680, 1994.

[41] S. Kang, S. Choi, and J.Y. Choi. View factor in cone calorimeter testing. *Int. J. Heat Mass Tran.*, 93:217–227, 2016.

[42] S. Kerber. Analysis of changing residential fire dynamics and its implications on firefighter operational timeframes. *Fire Technol.*, 48(4):865–891, 2012.

[43] A.J. Klinck. *An Experimental Investigation of the Fire Characteristics of the University of Waterloo Burn House Structure*. PhD thesis, University of Waterloo, Waterloo, ON, 2006.

[44] C.S. Lam and E.J. Weckman. Steady-state heat flux measurements in radiative and mixed radiative-convective environments. *Fire Mater.*, 33(7):303–321, 2009.

[45] C.W. Lautenberger. Gpyro3D: A three dimensional generalized pyrolysis model. In *Fire Saf. Sci. Proc. 11th Int. Sympos.*, pages 193–207, 2014.

[46] C.W. Lautenberger and C. Fernandez-Pello. Generalized pyrolysis model for combustible solids. *Fire Saf. J.*, 44(6):819–839, 2009.

[47] M. Lazaro, H. Bohmer, D. Alvear, J.A. Capote, and A. Trouve. Numerical simulation of fire growth, transition to flashover, and post-flashover dynamics in the dalmarnock fire test. *Fire Saf. Sci.*, 9:1377–1388, 2008.

[48] E.J. LeFevre and A.J. Ede. Laminar free convection from the outer surface of a vertical cylinder. In *Proc. 9th Int. Cong. Appl. Mech.*, pages 175–183, Brussels, Belgium, 1956. Free University of Brussels.

[49] N.C. Markatos, M.R. Malin, and G. Cox. Mathematical modelling of buoyancy-induced smoke flow in enclosures. *Int. J. Heat Mass Tran.*, 25(1):63–75, 1982.

[50] B.J. McBride, S. Gordon, and M.A. Reno. Coefficients for calculating thermodynamic and transport properties of individual species. *NASA (1993)*, 1993.

[51] R. McDermott, K.B. McGrattan, and J. Floyd. A simple reaction time scale for under-resolved fire dynamics. *Fire Saf. Sci.*, 10:809–820, 2011.

[52] K. McGrattan, S. Hostikka, J. Floyd, H. Baum, R. Rehm, W. Mell, and R. McDermott. Fire dynamics simulator (version 5), technical reference guide. *NIST special publication*, 1018(5), 2004.

[53] K.B. McGrattan, J. Floyd, G.P. Forney, H.R. Baum, and S. Hostikka. Improved radiation and combustion routines for a large eddy simulation fire model. *Fire Saf. Sci.*, 7:827–838, 2003.

[54] V. Novozhilov. Computational fluid dynamics modeling of compartment fires. *Prog. Energy Combust. Sci.*, 27(6):611–666, 2001.

[55] R.D. Peacock, W. Jones, P. Reneke, and G. Forney. Cfast–consolidated model of fire growth and smoke transport (version 6) users guide. *NIST Special Publication*, 1041, 2005.

[56] O. Pettersson, S.E. Magnuson, and J. Thor. Fire engineering design of structures., Swedish Institute of Steel Construction, 1976.

[57] S.B. Pope. *Turbulent flows*. Cambridge University Press, 2000.

[58] S. Porter. *Great Fire of London*. The History Press, 2011.

[59] J.G. Quintiere. Fire behavior in building compartments. *Proc. Combust. Instit.*, 29(1):181–193, 2002.

[60] J.G. Quintiere. *Principles of fire behavior*. CRC Press, 2016.

[61] M. Redmond and A.J. Mastropietro. Thermophysical and optical properties of materials considered for use on the ldsd test vehicle. In *ICES 2015 - Proc. 45th Int. Conf. Environ. Sys.*, Bellevue, WA, 2015. Texas Tech University.

[62] N. Ryder and E. Weckman. Effects on convective heat transfer coefficient in predictions of materials properties from cone calorimeter testing. Fire Mater. 13th In. Conf. Exhibit., 2013.

[63] P. Sagaut. *Large eddy simulation for incompressible flows: an introduction*. Springer Science & Business Media, 2006.

[64] D. Sahu, S. Jain, A. Gupta, and Shashi. Experimental study on methanol pool fires under low ventilated compartment. *Procedia Earth Planet. Sci.*, 11:507–515, 2015.

[65] D. Sahu, S. Kumar, S. Jain, and A. Gupta. Experimental and numerical simulation studies on diesel pool fire. *Fire Mater.*, 40(8):1016–1035, 2016.

[66] A. Schaelin, J. Van der Maas, and A. Moser. Simulation of airflow through large openings in buildings. *T Am. Soc. Heat. Refrig. Air Condition. Eng.*, 98:319–319, 1993.

[67] Siemens. Star CCM+ v12.2, 2018.

[68] R.F. Simmons. Fire chemistry, ch. 7, Combustion fundamentals of fire, G. Cox, ed, 1995.

[69] S. Sinha, A. Jhalani, M.R. Ravi, and A. Ray. Modelling of pyrolysis in wood: a review. *SESI J.*, 10(1):41–62, 2000.

[70] A.Y. Snegirev, V.A. Talalov, V.V. Stepanov, and J.N. Harris. A new model to predict pyrolysis, ignition and burning of flammable materials in fire tests. *Fire Saf. J.*, 59:132–150, 2013.

[71] J.E.J. Staggs. Convection heat transfer in the cone calorimeter. *Fire Saf. J.*, 44(4):469–474, 2009.

[72] J.E.J. Staggs. A reappraisal of convection heat transfer in the cone calorimeter. *Fire Saf. J.*, 46(3):125–131, 2011.

[73] K.D. Steckler, J.G. Quintiere, and W.J. Rinkinen. Flow induced by fire in a compartment. In *Int. Sympos. Combust.*, volume 19, pages 913–920. Elsevier, 1982.

[74] S.I. Stoliarov, I.T. Leventon, and R.E. Lyon. Two-dimensional model of burning for pyrolyzable solids. *Fire Mater.*, 38:391–408, 2014.

[75] S.I. Stoliarov and R.E. Lyon. Thermo-kinetic model of burning. *Federal Aviation Administration*, 2008.

[76] H. Takeda and J.R. Mehaffey. Wall2d: A model for predicting heat transfer through wood-stud walls exposed to fire. *Fire Mater.*, 22(4):133–140, 1998.

[77] A. Trouvé and Y. Wang. Large eddy simulation of compartment fires. *Int. J. Comput. Fluid D.*, 24(10):449–466, 2010.

[78] W. Tsang and R.F. Hampson. Chemical kinetic data base for combustion chemistry. part i. methane and related compounds. *J. Phys. and Chem. Ref. Data*, 15(3):1087–1279, 1986.

[79] P. Van Hees. Validation and verification of fire models for fire safety engineering. *Procedia Engineer.*, 62:154–168, 2013.

[80] H.K. Versteeg and W. Malalasekera. *An introduction to computational fluid dynamics: the finite volume method*. Pearson Education, 2007.

[81] S. Vilfayeau, N. Ren, Y. Wang, and A. Trouvé. Numerical simulation of under-ventilated liquid-fueled compartment fires with flame extinction and thermally-driven fuel evaporation. *Proc. Combust. Inst.*, 35(3):2563–2571, 2015.

[82] K. Wakatsuki. *High temperature radiation absorption of fuel molecules and an evaluation of its influence on pool fire modeling*. PhD thesis, University of Maryland, 2005.

[83] H. Wang. *Heat transfer analysis of components of construction exposed to fire*. PhD thesis, University of Salford, 1995.

[84] Y. Wang, P. Chatterjee, and J.L. de Ris. Large eddy simulation of fire plumes. *Proc. Combust. Inst.*, 33(2):2473–2480, 2011.

[85] C.K. Westbrook and F.L. Dryer. Simplified reaction mechanisms for the oxidation of hydrocarbon fuels in flames. *Combust. Sci. Technol.*, 27(1-2):31–43, 1981.

[86] M.T. Wilson, B.Z. Dlugogorski, and E.M. Kennedy. Uniformity of radiant heat fluxes in cone calorimeter. *Fire Saf. Sci.*, 7:815–826, 2003.

[87] A. Yoshizawa and K. Horiuti. A statistically-derived subgrid-scale kinetic energy model for the large-eddy simulation of turbulent flows. *J. Phys. Soc. Jpn.*, 54(8):2834–2839, 1985.

[88] C.A. Zaror and D.L. Pyle. The pyrolysis of biomass: A general review. *Proc. Ind. Acad. Sci. Sect. C: Eng. Sci.*, 5(4):269, 1982.

[89] J. Zhang and M.A Delichatsios. Determination of the convective heat transfer coefficient in three-dimensional inverse heat conduction problems. *Fire Saf. J.*, 44(5):681–690, 2009.